

# Characteristics of synchrotron radiation

Kwang-Je Kim



*AIP Conference Proceedings* 184, 565–632 (1989)

<https://doi.org/10.1063/1.38046>



CrossMark

## Articles You May Be Interested In

On the calculation of polyatomic Franck–Condon factors: Application to the  $^1A_{1g} \rightarrow ^1B_{2u}$  absorption band of benzene

*J. Chem. Phys.* (July 2008)

Anomalous electron streaming due to waves in tokamak plasmas

*AIP Conference Proceedings* (October 1994)

Quasi-regular solutions to a class of 3D degenerating hyperbolic equations

*AIP Conference Proceedings* (November 2012)



## Time to get excited.

Lock-in Amplifiers – from DC to 8.5 GHz



Find out more



# CHARACTERISTICS OF SYNCHROTRON RADIATION

Kwang-Je Kim

*Center for X-ray Optics  
Accelerator and Fusion Research Division  
Lawrence Berkeley Laboratory, Berkeley, CA 94720*

## TABLE OF CONTENTS

1	Introduction .....	567
2	Radiation by Relativistic Electrons .....	571
2.1	Emitter Time and Observer Time .....	571
2.2	The Scale-Change Factor $\kappa$ .....	572
2.3	Understanding Synchrotron Radiation .....	572
2.3.1	Time-Squeezing and Synchrotron Radiation .....	572
2.3.2	Qualitative Discussion of Bending-Magnet Radiation .....	573
2.3.3	Qualitative Discussion of Undulator Radiation .....	575
2.4	Radiation Formulae .....	576
2.4.1	General Formula .....	576
2.4.2	Far-Field Limit .....	576
2.4.3	Power and Flux .....	577
2.4.4	Coordinate System and Polarization Vectors .....	579
3	Bending-Magnet Radiation .....	581
3.1	Electron Orbit and Apparent Motion .....	581
3.2	Calculation of Angular Density of Spectral Flux .....	582
3.3	Angular Divergence .....	585
3.3.1	Simple Understanding .....	585
3.4	Polarization .....	587
3.5	Frequency-Integrated Power .....	588
4	Undulator Radiation .....	589
4.1	Electron Orbit and Apparent Motion .....	589
4.2	Spectral-Angular Characteristics .....	594
4.2.1	Spectrum at a Given Angle .....	595
4.2.2	Angular Pattern at a Given Frequency and Central Cone .....	596
4.2.3	The Peak Angular Density and the Flux in the Central Cone .....	599
4.2.4	Effect of Electrons' Angular Divergence .....	602
4.2.5	The Spectrum of the Angle-Integrated Flux .....	603

4.2.6	The Angular Distribution of the Frequency-Integrated Flux .....	605
4.3	Polarization .....	605
4.3.1	Special Undulators for Polarization Control .....	607
4.4	Frequency-Integrated Power .....	608
5	The Wiggler as a Large K Limit of an Undulator .....	611
6	Brightness, Coherence and Synchrotron Radiation Optics .....	615
6.1	Phase-Space Method in Geometric Optics .....	616
6.2	Phase-Space Method in Wave Optics .....	618
6.3	Gaussian Laser Beam .....	620
6.4	Effect of Electron Distribution on Brightness of Synchrotron Radiation .....	621
6.5	Brightness of Undulator Radiation .....	623
6.6	Brightness of Bending-Magnet and Wiggler Radiation .....	625
6.7	Coherence .....	626
	Acknowledgments .....	630
	References .....	631

# CHARACTERISTICS OF SYNCHROTRON RADIATION\*

Kwang-Je Kim

*Center for X-ray Optics  
Accelerator and Fusion Research Division  
Lawrence Berkeley Laboratory, Berkeley, CA 94720*

## 1 INTRODUCTION

Synchrotron radiation — the radiation produced by a charged particle moving with relativistic speed in curved trajectories — is playing an increasingly important role in many areas of basic and applied sciences. It provides intense, laser-like flux of photons in a wide range of spectral regions not accessible with other sources. In this paper, we review the principle of various synchrotron radiation sources and their characteristics.

There are three kinds of synchrotron radiation sources, bending magnets, wigglers, and undulators. These are illustrated in Fig. 1.1. In bending magnets, electrons move in a circular trajectory, producing a smooth spectrum. Wigglers can be regarded as a sequence of bending magnets of alternate polarities. Thus, the radiation characteristics are similar to those from bending magnets, apart from a  $2N$ -fold enhancement of the intensity, where  $2N$  is the number of the poles. An undulator is an  $N$ -period magnetic structure producing a gentle, periodic orbit. Because of the interference of radiation from different parts of the trajectory, the undulator radiation is squeezed into discrete spectrum and narrower emission angles. The result is an  $N^2$ -fold enhancement of the angular density of the flux in the forward direction. The spectral characteristics of radiation from bending magnets, wigglers and undulators are schematically illustrated and compared in Fig. 1.2.

An intrinsic characterization for the strength of a radiation source is the brightness, which is the flux per unit phase-space area, i.e., per unit source area per unit solid angle into which the radiation is emitted. High brightness means that the radiation can travel a long distance without significant spread, can be focused to a small spot, and can exhibit interference patterns. The brightness of the synchrotron radiation is being steadily increased thanks to the advance in the modern accelerator technology to build machines that store high-current, tightly focused, stable electron beams, and the development of strong and precise magnets that control the electron orbits for optimum production of radiation. In Fig. 1.3, the brightness of current and future synchrotron radiation sources is compared with that of the more traditional sources over the photon energy range extending from several eV to several tens of keV. It is seen that the synchrotron radiation is

---

\*This work was supported by the Director, Office of Energy Research, Office of Basic Energy Sciences, Material Sciences Division and Advanced Energy Projects Division, of the U.S. Department of Energy under Contract No. DE-AC03-76SF00098.

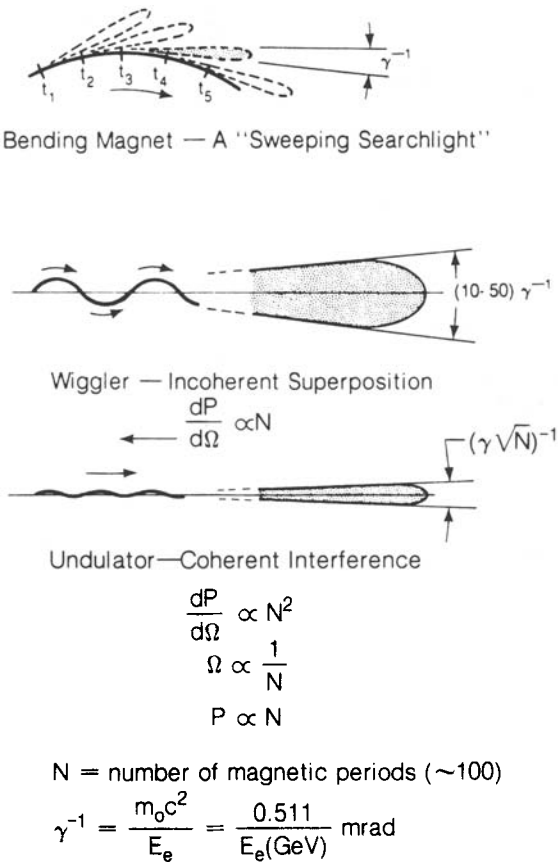


Figure 1.1 Schematic of three types of synchrotron radiation sources: bending magnet, wiggler and undulators.

brighter at least by two orders of magnitude for bending magnets in existing facilities and up to ten orders of magnitude for undulators in the future facilities.

In Section 2, we review the basic mechanism of generating synchrotron radiation. We explain how the apparent motion seen by a stationary observer appears to be contracted in time, resulting in a greatly enhanced acceleration in the extreme relativistic case [Feynman, 1963]. The physical picture emerging from this “time squeezing effect” leads to a qualitative understanding for the frequency and the intensity characteristics of synchrotron radiation, as well as the distinction between bending magnets and undulators. The section also contains general formulae that are the basis of calculations in later sections.

The following three sections are concerned with the radiation properties at a large distance from the sources. These properties can be analyzed by means of the standard radiation formula. The discussion of the radiation properties at an arbitrary distance, for example the brightness, requires a more general framework and is deferred until Section 6.

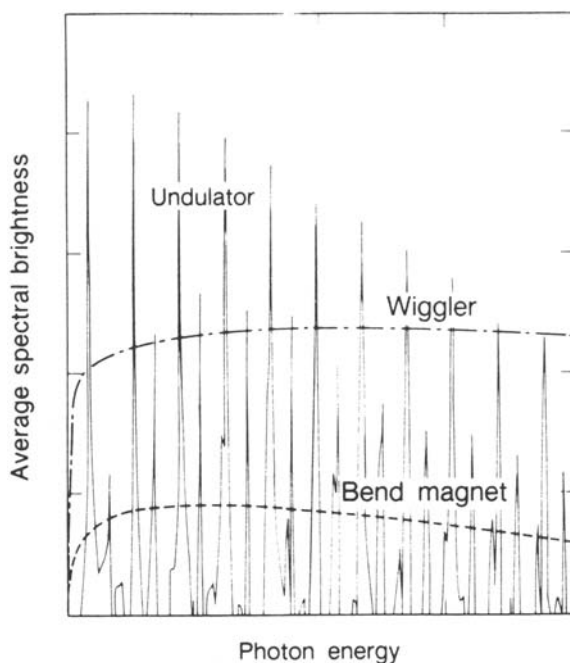


Figure 1.2 An illustration of different spectral characteristics of radiation from bending magnets, wigglers and undulators.

Section 3 contains a discussion of the bending-magnet radiation. The topics include the spectral characteristics, the angular distribution, the polarization, and the frequency-integrated power. An understanding of the wavelength dependence of the emission angle is provided using a simple physical argument.

In Section 4, we analyze the undulator radiation. The topics include the undulator harmonics, the spectrum at a given angle, the angular distribution at a given frequency, the effect due to the electron beam distribution, the angle-integrated spectrum, the frequency-integrated power, and the polarization. In addition to mathematical analysis, we emphasize physical understanding based on the properties of the apparent trajectories. Thus, the spectral shape, the strength of higher harmonics, the relation between the symmetry of the trajectory and the presence of even harmonics or the polarization properties are discussed from that point of view.

In Section 5, we discuss the wiggler as a limiting case of an undulator for a large orbit excursion. We establish the conditions under which a wiggler may be regarded as a sequence of bending magnets.

In Section 6, we return to a more general discussion and study the properties of synchrotron at finite distances, how it propagates through optical medium, how it forms interference patterns, etc. These topics have not been treated extensively in literature except for approximate arguments based on geometric optics [Green, 1976]. We discuss a more complete approach here based on a phase-space formulation of wave optics, in which the so-called brightness distribution function plays a

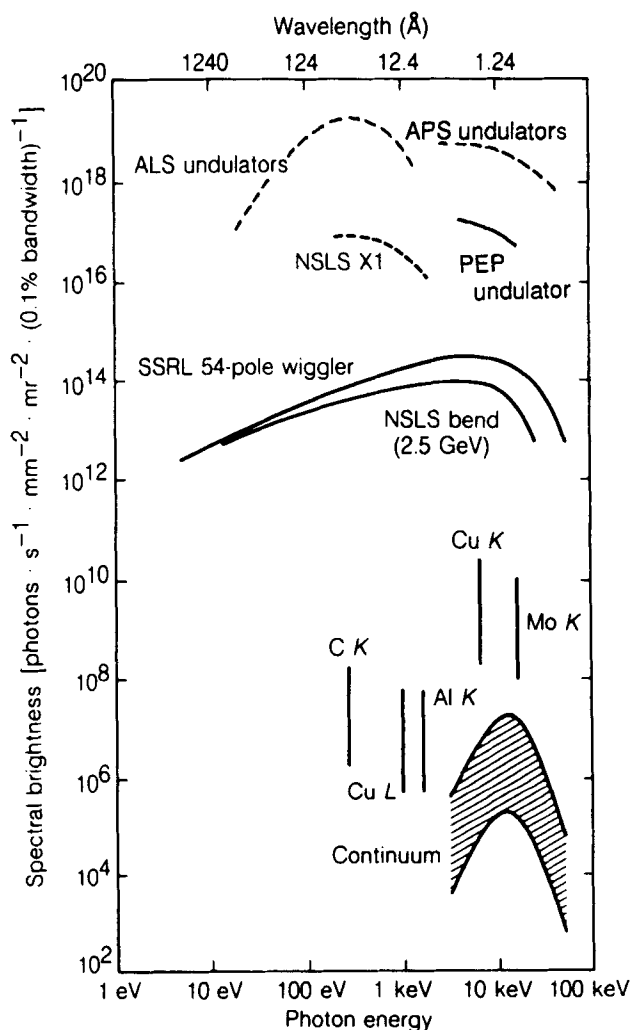


Figure 1.3 Spectral brightness for several synchrotron radiation sources and conventional x-ray sources. The data for conventional x-ray tubes should be taken as rough estimates only, since the brightness depends strongly on such parameters as operating voltage and take-off angle.

central role. We discuss the effect of electron beam in terms of a convolution theorem involving electron distribution and the brightness distribution, the radiation propagation by transformation of the brightness distribution function, and the coherence in terms of a criterion on phase-space area. Exact calculation of the brightness distribution function for synchrotron radiation is complicated. We describe approximate analysis in which the synchrotron radiation is replaced by Gaussian laser beam and which provides useful quantitative information on the optical properties of synchrotron radiation.

An account of works at the turn of the century on radiation by moving charges, leading to the theoretical understanding [Schwinger, 1949] and experimental observation of blue light from the GE synchrotron, can be found in Blewett (1988). Some of the previous reviews on synchrotron radiation characteristics are reported by Sokolov and Ternov (1966), Green (1976), Coisson (1979), Winick (1980), Hofmann (1980), and Krinsky, Perlman and Watson (1983).

## 2 RADIATION BY RELATIVISTIC ELECTRONS

The unique property of synchrotron radiation has its origin in the fact that, for an electron moving with a speed close to the speed of light toward a stationary observer, the motion appears to occur on a time scale much shorter than that of the real motion [Feynman, 1963]. In this section we discuss the general properties of the radiation from a relativistic electron based on this apparent motion.<sup>†</sup>

### 2.1 Emitter Time and Observer Time

Consider a relativistic electron moving on an arbitrary trajectory and a stationary observer as shown in Fig. 2.1. Let  $\mathbf{r}(t')$  be the position of the electron at time  $t'$ , and  $\mathbf{x}$  the position of the observer; then  $\mathbf{R}(t') = \mathbf{x} - \mathbf{r}(t')$  and  $R(t') = |\mathbf{R}(t')|$ . An electromagnetic signal emitted by the electron at time  $t'$  and traveling on a straight path will arrive at the observer at time

$$t = t' + R(t')/c, \quad (2.1)$$

where  $c$  is the speed of light.

Equation (2.1) relates two times,  $t$  and  $t'$ . The time  $t$  will be referred to as the observer time. The time  $t'$  is usually known by the somewhat mysterious name, "the retarded time." Here we will call it the emitter time in order to make the contrast with the observer time clearer. The electron motion in space is specified by a

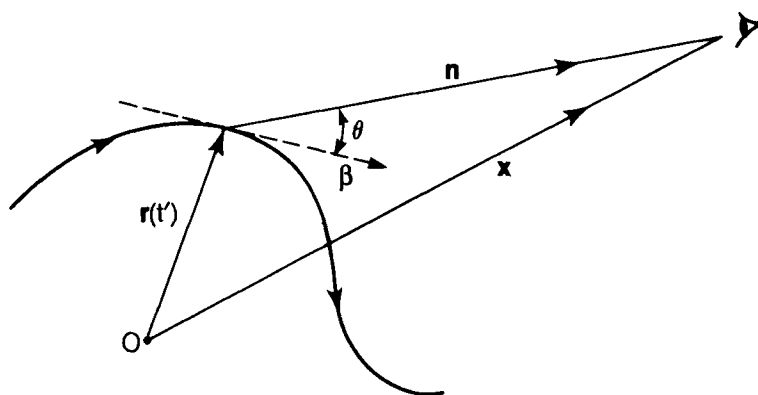


Figure 2.1 The electron trajectory and a stationary observer.

<sup>†</sup>Throughout this paper, we mean by an electron either an electron or a positron.



function  $\mathbf{r}(t')$  in terms of the emitter time. The motion appears different to the stationary observer; the apparent motion in terms of the observer time is obtained from the real motion by stretching or squeezing the time axis according to Eq. (2.1):

$$\mathbf{r}_a(t) = \mathbf{r}(t'(t)) \quad , \quad (2.2)$$

where  $t'(t)$  is a solution of Eq. (2.1).

To see how the time scales change, let  $\Delta t'$  be a small time interval in  $t'$  and  $\Delta t$  the corresponding interval in  $t$ . We have

$$\Delta t \approx \kappa(t') \Delta t' \quad , \quad (2.3)$$

$$\kappa(t') = \frac{dt}{dt'} = 1 - \mathbf{n}(t') \cdot \boldsymbol{\beta}(t') \quad . \quad (2.4)$$

Here  $\mathbf{n}(t')$  is a unit vector directed from  $\mathbf{r}(t')$  to the observer and  $c\boldsymbol{\beta}(t')$  is the instantaneous electron velocity. The function  $\kappa(t')$  is the  $t'$ -dependent scale-change factor.

## 2.2 The Scale-Change Factor $\kappa$

Let  $\theta$  be the angle between  $\mathbf{n}$  and  $\boldsymbol{\beta}$ . We have

$$\kappa = 1 - \beta \cos \theta \quad , \quad (2.5)$$

where  $\beta$  is the magnitude of  $\boldsymbol{\beta}$ . For the phenomena of interest in this paper, the electron speed is extremely relativistic, so that

$$1 - \beta = 1 - \sqrt{1 - \frac{1}{\gamma^2}} \approx \frac{1}{2\gamma^2} \ll 1 \quad , \quad (2.6)$$

where  $\gamma = E_e/m_e c^2$ ,  $E_e$  the electron's relativistic kinetic energy and  $m_e$  its mass. In practical units

$$\gamma = 1957 E_e [\text{GeV}] \quad .$$

For synchrotron radiation purposes,  $\gamma$  is typically a few thousands corresponding to an  $E_e$  of about a few GeV.

In the extreme relativistic case,  $\kappa$  depends sensitively on  $\theta$ . From Eqs. (2.5) and (2.6), we obtain

$$\begin{aligned} \kappa &\sim O(1) \quad ; \theta \sim 1 \quad , \\ \kappa &\approx \frac{1}{2} \left( \frac{1}{\gamma^2} + \theta^2 \right) \quad ; \theta \ll 1 \quad . \end{aligned} \quad (2.7)$$

## 2.3 Understanding Synchrotron Radiation

### 2.3.1 Time-Squeezing and Synchrotron Radiation

From Eqs. (2.3) and (2.7), we see that the scale difference in the emitter time and the observer time is greatest when  $\theta \lesssim \gamma^{-1}$ :

$$\Delta t \sim \Delta t' / \gamma^2 ; \theta \lesssim \gamma^{-1} . \quad (2.8)$$

In other words, when the electron velocity is pointing to the observer within an angle  $\gamma^{-1}$ , the electron motion in a time interval  $\Delta t'$  appears to the observer squeezed into a much shorter interval given by Eq. (2.8). At larger angles, this time-squeezing effect is not as significant.

The time-squeezing effect [Eq. (2.8)] is due essentially to the fact that a relativistic electron follows very closely behind the photons it emitted at earlier times. Therefore, the photons emitted at later times will follow closely behind the photons emitted earlier. Suppose the electron travels with a speed exactly equal to  $c$  toward an observer. Then the signals emitted at two different points along the trajectory will reach the observer at the same time. In this case, the time squeezing will be infinite  $[(\Delta t = 0)!]$ .

The strength of the electric field at the observer is proportional to the apparent acceleration of the motion seen by the observer. The apparent acceleration will be large when the time-squeezing effect is large. Thus, a large amount of the radiation will be observed when the relation between the electron motion and the observation direction is such that the time-squeezing effect is maximum. This is the basic explanation of the generation of synchrotron radiation.

### 2.3.2 Qualitative Discussion of Bending Magnet Radiation

Consider an electron trajectory and an observer in the forward direction, as shown in Fig. 2.2a. Significant time-squeezing occurs in a small portion of the trajectory AB around the point P tangent to the observation direction in which the slope of the trajectory is within an angle  $\gamma^{-1}$  with respect to the observation direction. Since  $\gamma^{-1}$  is small, typically a fraction of milliradians, the curve in this portion can be approximated by a circle whose radius is equal to the radius of the curvature  $\rho$  [Schwinger, 1949]. The radiation from such a curve segment is essentially the same character as that from an electron traveling in a bending magnet.

In Figs. 2.2b and 2.2c, we show the transverse motion as a function of  $t'$  and of  $t$ , respectively. The points corresponding to P, A and B in Fig. 2.2a are marked with the same symbols. In terms of the emitter time, the electron moves between A and B in a time  $\Delta t' \sim 2\rho/\gamma c$  with a transverse amplitude variation  $\Delta x \sim \rho/\gamma^2$ . In terms of the observer time, the motion happens in a much shorter interval  $\Delta t \sim \Delta t'/\gamma^2 = 2\rho/\gamma^3 c$ . Thus, the apparent motion seen by the observer will be schematically as shown in Fig. 2.2c. The sharp kink in the trajectory at P gives rise to a very large apparent acceleration:

$$\frac{d^2x}{dt^2} \sim \frac{\Delta x}{(\Delta t)^2} \sim \gamma^4 \frac{c^2}{\rho} . \quad (2.9)$$

Compared to the acceleration in terms of the emitter time  $t'$ , this is larger by a factor  $\gamma^4$ , which is larger than  $10^{12}$  in typical cases!

The radiation at the observer depends on the acceleration of the apparent motion, as will be discussed later in Subsection 2.4. The enhanced apparent acceleration, Eq. (2.9), means therefore that a large amount of the radiation will be delivered to the observer from the portions of the electron trajectory that are nearly parallel to the observation direction. The angular opening of the radiation is nar-

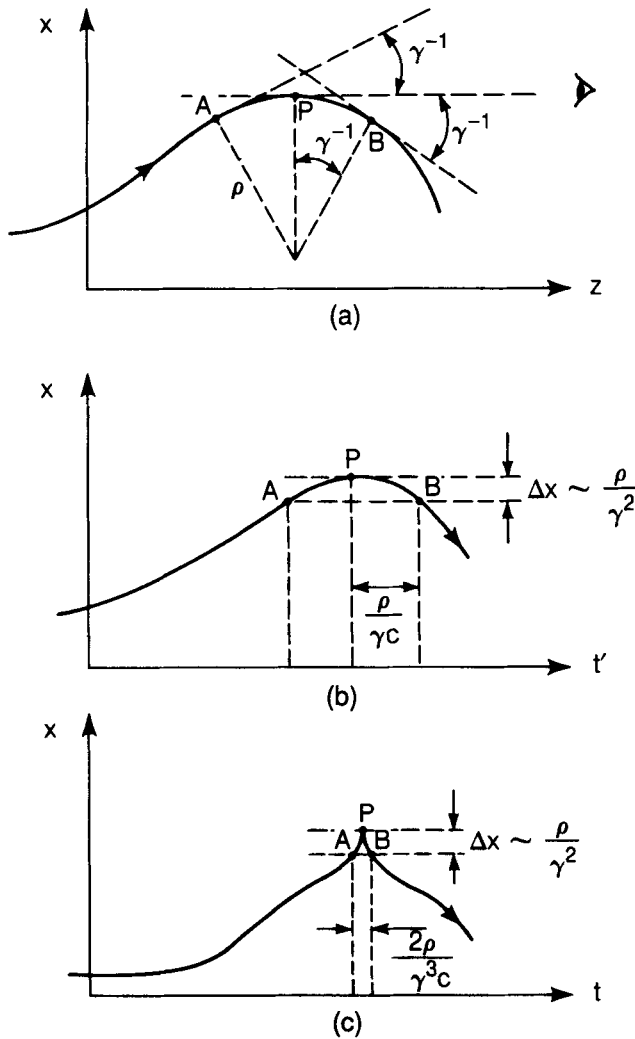


Figure 2.2 The electron trajectory in space (a), the electron trajectory as a function of the emitter time  $t'$  (b), and the apparent electron trajectory as a function of the observer time  $t$  (c). The trajectory slope at P is in the observation direction.

row, about  $\gamma^{-1}$ , because the time-squeezing is not significant beyond that angle. The typical frequency of the radiation will be very high, of the order  $\omega_{\text{typ}} \sim 1/\Delta t \sim \gamma^3 c/\rho$ . The picture emerging from this discussion is that a relativistic electron on a curved trajectory emits a narrow pencil of very intense radiation in the direction of the motion, as illustrated in Fig. 2.3.

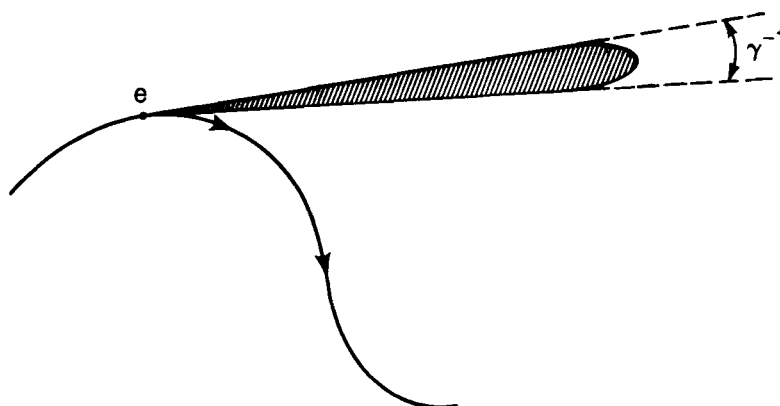


Figure 2.3 Synchrotron radiation as a narrow pencil of angular width  $\gamma^{-1}$ .

### 2.3.3 Qualitative Discussion of Undulator Radiation

Figure 2.4 shows another type of very interesting electron trajectories in a periodic magnetic field [Motz, 1951; Alferov et al., 1973; Kincaid, 1977]. For these trajectories the angle  $\theta$  between the trajectory slope and the observation direction is everywhere smaller than  $\gamma^{-1}$ . A periodic magnetic device called an undulator produces such an orbit. If the orbit is periodic with period length  $\lambda_u$ , the time squeezed signal will also be periodic. In the forward direction, the period length  $\lambda_1$  of the signal will be reduced in view of Eq. (2.7) by about  $2\gamma^2$  from  $\lambda_u$ :

$$\lambda_1 = \frac{\lambda_u}{2\gamma^2} (1 + \gamma^2 \langle \theta^2 \rangle) , \quad (2.10)$$

where  $\langle \theta^2 \rangle$  is the average of  $\theta^2$  in one period. The undulator radiation will then have sharp spectra at discrete frequencies corresponding to the harmonics of  $\lambda_1$ . For an  $N$ -period undulator, the radiation intensity will be higher by about  $2N$  compared to that from a single bending magnet. Moreover, we will see in Section 4 that the radiation opening angle at a given wavelength is smaller by about  $\sqrt{N}$  compared to that of the bending magnet due to the interference effect. Thus the radiation intensity per unit solid angle for an undulator will be higher by about  $N^2$ .

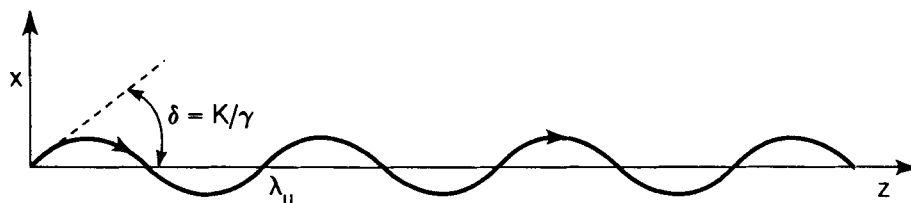


Figure 2.4 The electron trajectory in an undulator. The trajectory is periodic with period length  $\lambda_u$ .

## 2.4 Radiation Formulae

### 2.4.1 General Formula

The expression for the electric field  $\mathbf{E}$  at  $\mathbf{x}$  is derived in textbooks (see for example, Jackson, 1962):

$$\mathbf{E}(\mathbf{x}, t) = \frac{e}{4\pi\epsilon_0} \left[ \frac{1}{\kappa} \frac{\mathbf{n}}{R^2} + \frac{1}{c\kappa} \frac{d}{dt'} \left( \frac{\mathbf{n} - \boldsymbol{\beta}}{\kappa R} \right) \right] . \quad (2.11)$$

Here and in the following, the square brackets will be understood to mean that the quantities within the brackets are to be evaluated at the emitter time  $t'$ . See Eq. (2.1). The magnetic field is

$$\mathbf{B}(\mathbf{x}, t) = \frac{1}{c} \mathbf{n} \times \mathbf{E}(\mathbf{x}, t) . \quad (2.12)$$

By using the identity

$$\mathbf{n} - \boldsymbol{\beta} = \mathbf{n} \times (\mathbf{n} \times \boldsymbol{\beta}) + \kappa \mathbf{n} , \quad (2.13)$$

Eq. (2.9) can be written as

$$\mathbf{E}(\mathbf{x}, t) = \frac{e}{4\pi\epsilon_0} \left[ \frac{\mathbf{n}}{R^2} + \frac{R}{\kappa c} \frac{d}{dt'} \frac{\mathbf{n}}{R^2} + \frac{1}{c\kappa} \frac{d}{dt'} \frac{\mathbf{n} \times (\mathbf{n} \times \boldsymbol{\beta})}{\kappa R} \right] . \quad (2.14)$$

We remark in passing that Eq. (2.14) can be shown to be equivalent to the expression given by Feynman (1963) by using the relation

$$\frac{1}{c} \frac{d\mathbf{n}(t')}{dt'} = \frac{1}{R} \left[ \mathbf{n} \times (\mathbf{n} \times \boldsymbol{\beta}) \right] .$$

### 2.4.2 Far-Field Limit

The expression simplifies in the far-field limit

$$\mathbf{x} = \mathbf{n}R_0 ,$$

$$R_0 \rightarrow \infty ,$$

$$|\mathbf{r}(t')| / R_0 \rightarrow 0 .$$

In this case, we can regard  $\mathbf{n}$  to be a constant vector. Retaining only terms of order  $O(R_0^{-1})$ , we find

$$\lim R_0 \mathbf{E}(\mathbf{n}R_0, t) = \frac{e}{4\pi\epsilon_0 c^2} \mathbf{a} . \quad (2.15)$$

Here  $\lim$  implies taking the limit  $R_0 \rightarrow \infty$  and

$$\mathbf{a} = \mathbf{n} \times \left[ \mathbf{n} \times \frac{d^2}{dt^2} \mathbf{r}(t'(t)) \right] , \quad (2.16a)$$

$$= c\mathbf{n} \times \left[ \mathbf{n} \times \frac{1}{\kappa(t')} \frac{d}{dt'} \frac{1}{\kappa(t')} \boldsymbol{\beta}(t') \right] . \quad (2.16b)$$

In Eq. (2.16b), use was made of Eq. (2.4) to convert the  $t$ -derivatives into the  $t'$ -derivatives. In Eq. (2.16a), the quantity  $d^2\mathbf{r}(t')/dt'^2$  is the acceleration of the apparent motion seen by the observer. The vector  $\mathbf{a}$  is the projection of the acceleration into a line perpendicular to  $\mathbf{n}$  and in the plane defined by  $\mathbf{n}$  and the acceleration, as explained in Fig. 2.5. Equation (2.15) is the statement that the electric field at the observation point is proportional to the transverse component of the apparent acceleration. This fact was important for the discussions in Subsection 2.3. The appearance of  $\kappa$  in the denominators of Eq. (2.16b) implies that the apparent acceleration is large for small  $\kappa$ , in accordance with our discussion there.

In the far-field limit, Eq. (2.1) simplifies also:

$$t = t' - \mathbf{n} \cdot \mathbf{r}(t')/c . \quad (2.17)$$

Here we have removed a large but uninteresting constant,  $R_0/c$ , in the definition of  $t$ .

### 2.4.3 Power and Flux

The energy radiated per unit solid angle is given by

$$\begin{aligned} \frac{d^2W}{d^2\Omega} &= \epsilon_0 c \lim \int |R_0 \mathbf{E}(\mathbf{n}R_0, t)|^2 dt \\ &= \frac{e^2}{4\pi\epsilon_0} \frac{1}{4\pi c^3} \int |\mathbf{a}|^2 dt . \end{aligned} \quad (2.18)$$

To find the spectrum, we introduce the Fourier transform:

$$\mathbf{E}(\mathbf{x}, \omega) = \frac{1}{\sqrt{2\pi}} \int_{-\infty}^{\infty} dt \mathbf{E}(\mathbf{x}, t) e^{i\omega t} . \quad (2.19)$$

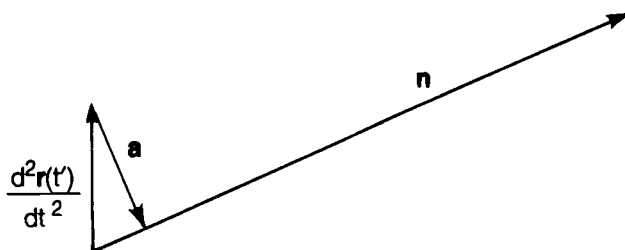


Figure 2.5 Explanation of the construction of the vector  $\mathbf{a}$  [Eq. (2.16a)].

Using the fact that

$$\begin{aligned}\int_{-\infty}^{\infty} |\mathbf{E}(\mathbf{x}, t)|^2 dt &= \int_{-\infty}^{\infty} |\mathbf{E}(\mathbf{x}, \omega)|^2 d\omega, \\ &= 2 \int_0^{\infty} |\mathbf{E}(\mathbf{x}, \omega)|^2 d\omega,\end{aligned}$$

Eq. (2.18) can be interpreted as

$$\frac{d^3W}{d\omega d^2\Omega} = 2\varepsilon_0 c \lim |\mathbf{R}_0 \mathbf{E}(\mathbf{nR}_0, \omega)|^2. \quad (2.20)$$

From Eqs. (2.15), (2.16), (2.19) and (2.20), and after integration by parts, we obtain

$$\frac{d^3W}{d\omega d^2\Omega} = \frac{e^2}{4\pi\varepsilon_0} \frac{1}{c} |\mathbf{A}(\omega)|^2, \quad (2.21)$$

where

$$\mathbf{A}(\omega) = \frac{\omega}{2\pi} \int_{-\infty}^{\infty} dt' \mathbf{n} \times \left[ \mathbf{n} \times \boldsymbol{\beta}(t') \right] e^{i\omega t(t')}. \quad (2.22)$$

Here the observer time  $t(t')$  in the exponent is given by Eq. (2.17).

So far, we have considered the radiation by a single electron. For a beam of parallel electrons with current  $I$ , Eq. (2.18) becomes

$$\frac{d^2P}{d^2\Omega} = \frac{e^2}{4\pi\varepsilon_0} \frac{1}{4\pi c^3} \frac{I}{e} \int |\mathbf{a}|^2 dt. \quad (2.23)$$

Here  $P$  is the radiated energy per unit time, i.e., the power. Equation (2.21) can be converted similarly. In this case, however, we will write the expression for the number of the radiated photons per unit time, the flux, by dividing the right-hand side by  $\hbar\omega$  ( $\hbar$  = Planck's constant): Let  $\mathcal{F}$  be the spectral flux into a small bandwidth  $\Delta\omega$ . We obtain

$$\frac{d^2\mathcal{F}}{d^2\Omega} = \alpha \frac{\Delta\omega}{\omega} \frac{I}{e} |\mathbf{A}(\omega)|^2, \quad (2.24)$$

where  $\alpha = e^2/4\pi\varepsilon_0\hbar c = 1/137$  is the fine-structure constant.

In Eqs. (2.23) and (2.24), the effects due to electrons' angular divergence are neglected. Those effects will be studied separately later when they become important.

The distribution of the spectral flux, Eq. (2.24), is an important quantity determining the usefulness of the photons in scientific experiments. The frequency-integrated power [Eq. (2.23)] is important in designing beam lines that transport the radiation from sources to the experimental area. Beam lines usually involve sensitive optical elements. Thus the power contained in the unwanted spectral regions should not be excessive so as to limit thermal loading on the optical elements.

We can do a simple calculation based on Eq. (2.18) to estimate the number of photons  $\Delta N_\gamma$  generated while the electron trajectory bends an angle  $\gamma^{-1}$ . The total radiated energy is

$$W \sim \frac{e^2}{4\pi\epsilon_0} \frac{1}{4\pi c^3} \left( \frac{d^2x}{dt^2} \right)^2 \Delta t \Delta\Omega ,$$

where  $\Delta\Omega$  is the solid angle.  $\Delta N_\gamma$  is obtained by dividing  $W$  by  $\hbar\omega_{\text{typ}}$  and

$$\Delta N_\gamma \sim \alpha \frac{1}{c^2\omega_{\text{typ}}} \cdot \Delta t \cdot \Delta\Omega \left( \frac{d^2x}{dt^2} \right)^2 .$$

Inserting  $\omega_{\text{typ}} \sim 1/\Delta t$ ,  $\Delta t \sim \rho/\gamma^3 c$ ,  $\Delta\Omega \sim \gamma^{-2}$ , and  $d^2x/dt^2$  by Eq. (2.9) one obtains

$$\Delta N_\gamma \sim \alpha . \quad (2.25)$$

For an electron beam, the total flux per  $\gamma^{-1}$  bending is

$$\Delta \mathcal{F} \sim \alpha \frac{I}{e} . \quad (2.26)$$

This is a large flux, about  $10^{16}$  photons per second per ampere. We are beginning to see why the synchrotron radiation is useful.

#### 2.4.4 Coordinate System and Polarization Vectors

We will be mainly interested in the case where the electron trajectory lies on a plane, and we assume this plane to be the horizontal plane. We choose the coordinate system as shown in Fig. 2-6: the main direction of the electron motion is along the  $z$ -direction, the  $x$ -axis is transverse to the main motion in the horizontal plane and the  $y$ -axis is in the vertical direction. Let the horizontal and vertical observation angles be respectively  $\phi$  and  $\psi$ . These angles are of the order  $\gamma^{-1}$ . Thus

$$\mathbf{n} = \left[ \phi, \psi, 1 - \frac{1}{2}(\phi^2 + \psi^2) \right] + O(\gamma^{-3}) . \quad (2.27)$$

The components of  $\beta$  are

$$\beta = (\beta_x, 0, \beta_z) . \quad (2.28)$$

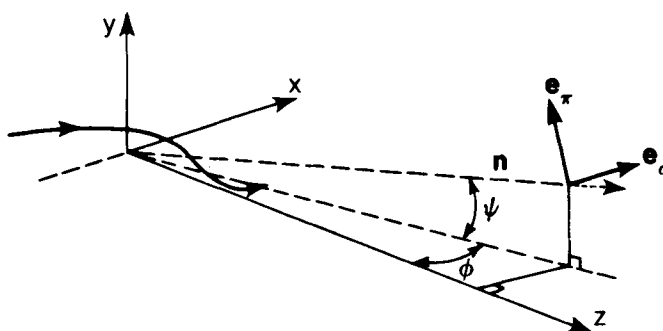


Figure 2.6 The coordinate system. The vector  $\mathbf{e}_\sigma$  lies in the horizontal plane. The triplet  $\mathbf{e}_\sigma$ ,  $\mathbf{e}_\pi$  and  $\mathbf{n}$  forms an orthonormal set.



Since  $\beta_x$  is of the order  $\gamma^{-1}$ , we have

$$\beta_z = 1 - \frac{1}{2\gamma^2} - \frac{1}{2}\beta_x^2 + O(\gamma^{-3}) . \quad (2.29)$$

It follows from these that

$$\kappa = 1 - \boldsymbol{\beta} \cdot \mathbf{n} \approx \frac{1}{2} \left[ (\beta_x - \varphi)^2 + \frac{1}{\gamma^2} + \psi^2 \right] . \quad (2.30)$$

Denoting the derivative with respect to the emitter time  $t'$  by a dot, we obtain

$$\dot{\boldsymbol{\beta}} \approx \left( \dot{\beta}_x, 0, -\beta_x \dot{\beta}_x \right) . \quad (2.31)$$

Therefore

$$\dot{\boldsymbol{\beta}} \cdot \mathbf{n} \approx \left( \varphi - \beta_x \right) \dot{\beta}_x . \quad (2.32)$$

The electric field is decomposed into two polarization components, the  $\sigma$ - and the  $\pi$ -components, by using the unit vectors  $\mathbf{e}_\sigma$  and  $\mathbf{e}_\pi$ . The triad  $\mathbf{e}_\sigma$ ,  $\mathbf{e}_\pi$  and  $\mathbf{n}$  forms an orthonormal set. Choosing  $\mathbf{e}_\sigma$  to lie in the horizontal plane, we have

$$\begin{aligned} \mathbf{e}_\sigma &= \mathbf{e}_x - \varphi \mathbf{e}_z + O(\gamma^{-2}) \\ \mathbf{e}_\pi &= \mathbf{e}_y - \psi \mathbf{e}_z + O(\gamma^{-2}) . \end{aligned} \quad (2.33)$$

The electric field, Eq. (2.15) or (2.22), is of the form

$$\mathbf{n} \times (\mathbf{n} \times \mathbf{b}) = (\mathbf{n} \cdot \mathbf{b}) \mathbf{n} - \mathbf{b} . \quad (2.34)$$

Its  $\sigma$ - and  $\pi$ -components are

$$\begin{aligned} \mathbf{n} \times (\mathbf{n} \times \mathbf{b}) |_\sigma &= (\mathbf{n} \cdot \mathbf{b} \varphi - b_x) - \varphi (\mathbf{n} \cdot \mathbf{b} n_z - b_z) \\ \mathbf{n} \times (\mathbf{n} \times \mathbf{b}) |_\pi &= (\mathbf{n} \cdot \mathbf{b} \psi - b_y) - \psi (\mathbf{n} \cdot \mathbf{b} n_z - b_z) . \end{aligned} \quad (2.35)$$

To calculate the electric field in the time domain, we need to evaluate Eq. (2.16). Thus we set

$$\mathbf{b} \rightarrow \frac{1}{\kappa} \frac{d}{dt'} \frac{\boldsymbol{\beta}}{\kappa} = \frac{\dot{\boldsymbol{\beta}} \kappa + (\mathbf{n} \cdot \dot{\boldsymbol{\beta}}) \boldsymbol{\beta}}{\kappa^3} , \quad (2.36)$$

where the dots represent taking the derivative with respect to the emitter time  $t'$ . The components of Eq. (2.36) retaining only the leading terms are

$$\mathbf{b} = \frac{1}{\kappa^3} \left( \kappa + (\varphi - \beta_x) \beta_x, 0, (\varphi - \beta_x) \right) \dot{\beta}_x . \quad (2.37)$$

Inserting this into Eq. (2.35), we find that the terms that come from  $\varphi \mathbf{e}_z$  and  $\psi \mathbf{e}_z$  in Eq. (2.33) are negligible. That is,  $\mathbf{e}_\sigma$  and  $\mathbf{e}_\pi$  may be approximated by  $\mathbf{e}_x$  and  $\mathbf{e}_y$ , respectively. The result is

$$\begin{aligned} \mathbf{n} \times (\mathbf{n} \times \mathbf{b}) |_\sigma &\approx \mathbf{n} \times (\mathbf{n} \times \mathbf{b}) |_x \approx \frac{(\varphi - \beta_x)^2 \dot{\beta}_x - \kappa \dot{\beta}_x}{\kappa^3} \\ \mathbf{n} \times (\mathbf{n} \times \mathbf{b}) |_\pi &\approx \mathbf{n} \times (\mathbf{n} \times \mathbf{b}) |_y \approx \frac{\psi (\varphi - \beta_x) \dot{\beta}_x}{\kappa^3} . \end{aligned} \quad (2.38)$$

Thus Eq. (2.23) becomes

$$\left( \frac{d P_\sigma}{d\Omega} \right) = \frac{e^2}{4\pi\epsilon_0} \frac{1}{4\pi c} \frac{I}{e} \int dt' \frac{\dot{\beta}_x^2}{\kappa^5} \left[ \frac{(\varphi - \beta_x)^2 - \kappa^2}{\psi^2(\varphi - \beta_x)^2} \right] . \quad (2.39)$$

For the electric field in the frequency domain [Eq. (2.22)] we replace  $\mathbf{b} \rightarrow \boldsymbol{\beta}$ . Again, we find that the  $\sigma$ - and the  $\pi$ -components can be approximated by the  $x$ - and the  $z$ -components, and we find

$$\begin{aligned} \mathbf{n} \times (\mathbf{n} \times \boldsymbol{\beta})|_\sigma &\approx \mathbf{n} \times (\mathbf{n} \times \boldsymbol{\beta})|_x \approx \varphi - \beta_x \\ \mathbf{n} \times (\mathbf{n} \times \boldsymbol{\beta})|_\pi &\approx \mathbf{n} \times (\mathbf{n} \times \boldsymbol{\beta})|_y \approx \psi . \end{aligned} \quad (2.40)$$

Therefore, Eq. (2.22) and (2.24) becomes

$$\frac{d^2 \mathcal{F}_{\sigma,\pi}}{d^2\Omega} = \alpha \frac{\Delta\omega}{\omega} \frac{I}{e} |A_{\sigma,\pi}(\omega)|^2 , \quad (2.41)$$

$$\begin{pmatrix} A_\sigma(\omega) \\ A_\pi(\omega) \end{pmatrix} = \frac{\omega}{2\pi} \int_{-\infty}^{\infty} dt' \begin{pmatrix} \varphi - \beta_x \\ \psi \end{pmatrix} e^{i\omega t'(t)} . \quad (2.42)$$

### 3 BENDING-MAGNET RADIATION

#### 3.1 Electron Orbit and Apparent Motion

For an electron following a circular trajectory (as in the bending magnets of a storage ring) the bending radius, in the extreme relativistic case, is given by

$$\rho = \frac{E_e}{ecB} = \frac{m_e c \gamma}{eB} , \quad (3.1)$$

where  $B$  is the magnetic field strength. In practical units this becomes

$$\rho[\text{m}] = 3.3 E_e [\text{GeV}] / B[\text{T}] .$$

Typically,  $\rho$  is a few meters. The angular speed is

$$\omega_p = \frac{\beta c}{\rho} \approx \frac{c}{\rho} . \quad (3.2)$$

The coordinate system is as shown in Fig. 3.1. For a circular motion, the observation directions different in horizontal angle are equivalent, thus we may set  $\varphi = 0$ . The electron trajectory in terms of the emitter time  $t'$  is

$$\begin{aligned} \mathbf{r}(t') &= \rho \left( 1 - \cos(\omega_p t'), 0, \sin(\omega_p t') \right) , \\ \boldsymbol{\beta}(t') &= \beta \left( \sin(\omega_p t'), 0, \cos(\omega_p t') \right) . \end{aligned} \quad (3.3)$$

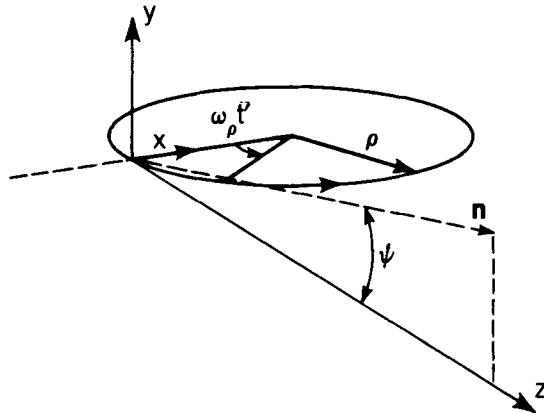


Figure 3.1 The orbit and the coordinate system for bending-magnet radiation.

We evaluate the time-squeeze factor  $\kappa(t')$  given by Eq. (2.4). Since the angle between  $\beta$  and  $n$  is  $\omega_p t'$  horizontally and  $\psi$  vertically, we have

$$\theta^2 = \psi^2 + \omega_p^2 t'^2 .$$

It then follows from Eq. (2.7) that

$$\kappa(t') = \frac{dt}{dt'} = \frac{1}{2} \left[ \frac{1}{\gamma^2} + \psi^2 + \omega_p^2 t'^2 \right] . \quad (3.4)$$

Integrating this we obtain

$$t(t') = \frac{1}{2} \left[ \frac{1}{\gamma^2} + \psi^2 \right] t' + \frac{\omega_p^2 t'^3}{6} . \quad (3.5)$$

Equation (3.5) can also be obtained by replacing the trajectory equation [Eq. (3.3)] in Eq. (2.17) and expanding the result in angles.

The apparent motion in  $t$  can be obtained from Eqs. (3.3) and (3.5). It is left as an exercise to the reader to verify the sharp kink in the apparent motion qualitatively illustrated in Fig. 2.2c.

### 3.2 Calculation of Angular Density of Spectral Flux [Schwinger (1949), Jackson (1962), Sokolov and Ternov (1968)]

We insert Eqs. (3.3) and (3.5) into Eq. (2.42)

$$\left( \frac{A_\sigma}{A_\pi} \right) = \frac{\omega}{2\pi} \int_{-\infty}^{\infty} dt' \left[ \begin{matrix} -\sin \omega_p t' \\ \psi \end{matrix} \right] \exp \left[ i\omega t(t') \right] dt' . \quad (3.6)$$

Introducing the critical frequency  $\omega_c$

$$\omega_c = \frac{3}{2} \gamma^3 \omega_p = \frac{3\gamma^3 c}{2\rho} , \quad (3.7)$$

the exponent in the integrand of Eq. (3.6) becomes

$$\omega t(t') = \frac{3\eta}{2} \left[ \tau + \frac{\tau^3}{3} \right] . \quad (3.8)$$

Here

$$\eta = \frac{1}{2} \frac{\omega}{\omega_c} (1 + X^2)^{3/2} ,$$

$$X = \gamma\psi , \quad (3.9)$$

and we have introduced a new integration variable

$$\tau = \gamma\omega_p t' / \sqrt{1 + X^2} . \quad (3.10)$$

The integrals in Eq. (3.6) can be expressed as the modified Bessel functions:

$$K_{2/3}(\eta) = \sqrt{3} \int_0^\infty \tau \sin \left[ \frac{3}{2} \eta \left( \tau + \frac{1}{3} \tau^3 \right) \right] d\tau$$

$$K_{1/3}(\eta) = \sqrt{3} \int_0^\infty \cos \left[ \frac{3}{2} \eta \left( \tau + \frac{1}{3} \tau^3 \right) \right] d\tau .$$

The result is

$$\begin{pmatrix} A_\sigma \\ A_\pi \end{pmatrix} = \frac{\sqrt{3}}{2\pi} \gamma \frac{\omega}{\omega_c} (1 + X^2)(-i) \begin{pmatrix} K_{2/3}(\eta) \\ \frac{iX}{\sqrt{1+X^2}} K_{1/3}(\eta) \end{pmatrix} . \quad (3.11)$$

Inserting this into Eq. (2.41), we finally obtain the angular density of the spectral flux:

$$\begin{pmatrix} \frac{d^2 \mathcal{F}_\sigma}{d^2 \Omega} \\ \frac{d^2 \mathcal{F}_\pi}{d^2 \Omega} \end{pmatrix} = \frac{3\alpha}{4\pi^2} \gamma^2 \frac{\Delta\omega}{\omega} \frac{1}{e} \left( \frac{\omega}{\omega_c} \right)^2 (1 + X^2)^2 \begin{pmatrix} K_{2/3}^2(\eta) \\ \frac{X^2}{1 + X^2} K_{1/3}^2(\eta) \end{pmatrix} . \quad (3.12)$$

In the forward direction,  $\psi = 0$ , the flux for the  $\pi$ -component vanishes. In practical units [photons  $\cdot$  s $^{-1}$   $\cdot$  mr $^{-2}$   $\cdot$  (0.1% bandwidth) $^{-1}$ ], this becomes

$$\left. \frac{d^2 \mathcal{F}}{d^2 \Omega} \right|_{\psi=0} = 1.33 \times 10^{13} E_e^2 [\text{GeV}] I[A] H_2(\omega/\omega_c) , \quad (3.13)$$

where  $\varphi$  is the horizontal angle and

$$H_2(y) = y^2 K_{2/3}^2(y/2) . \quad (3.14)$$

The function  $H_2(y)$  is shown in Fig. 3.2. The bending-magnet radiation has a smooth spectral distribution, with a broad maximum near the critical frequency  $\omega_c$ . The photon energy corresponding to  $\omega_c$ ,  $\varepsilon_c = \hbar\omega_c$  is in practical units

$$\varepsilon_c [\text{keV}] = 0.665 E_e^2 [\text{GeV}] B [\text{T}] . \quad (3.15)$$

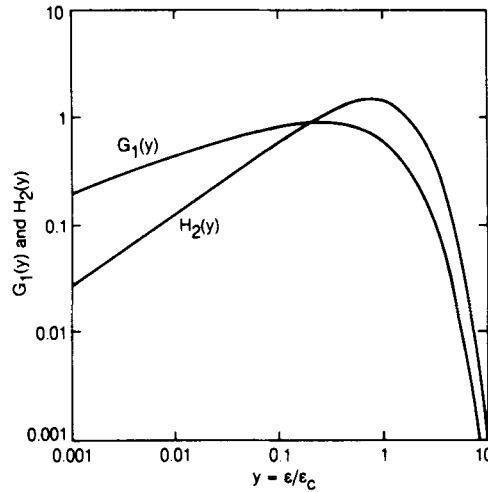


Figure 3.2 The functions  $G_1(y)$  and  $H_2(y)$ , where  $y$  is the ratio between the photon frequency and the critical photon frequency  $\omega_c$ .

Typically,  $\epsilon_c$  is several keV. The critical wavelength corresponding to  $\omega_c$  is

$$\lambda_c = \frac{4\pi\rho}{3\gamma^3} . \quad (3.16)$$

The asymptotic properties of the modified Bessel functions are

$$K_\nu(y) \rightarrow 2^{\nu-1} \Gamma(\nu) y^{-\nu} ; y \ll 1$$

$$\rightarrow \sqrt{\frac{\pi}{2y}} e^{-y} ; y \gg 1 . \quad (3.17)$$

Using this, we see that the angular density of the spectral flux vanishes as  $(\omega/\omega_c)^{2/3}$  for  $\omega \ll \omega_c$  and as  $\exp(-\omega/\omega_c)$  for  $\omega \gg \omega_c$ . It is customary to define  $4\omega_c$  as the upper limit of the useful photon frequency for the bending-magnet radiation.

Integrating Eq. (3.12) over the vertical angle  $\psi$ , we obtain

$$\left( \frac{d\mathcal{F}_\sigma}{d\phi} \right) = \frac{\sqrt{3}}{4\pi} \alpha\gamma \frac{\Delta\omega}{\omega} \frac{1}{e} \frac{\omega}{\omega_c} \left( \int_{\omega/\omega_c}^{\infty} K_{5/3}(y') dy' + K_{2/3}\left(\frac{\omega}{\omega_c}\right) \right) . \quad (3.18)$$

$$\left( \frac{d\mathcal{F}_\pi}{d\phi} \right) = \frac{\sqrt{3}}{4\pi} \alpha\gamma \frac{\Delta\omega}{\omega} \frac{1}{e} \frac{\omega}{\omega_c} \left( \int_{\omega/\omega_c}^{\infty} K_{5/3}(y') dy' - K_{2/3}\left(\frac{\omega}{\omega_c}\right) \right)$$

The Bessel function identities required to obtain the above equation can be found in Hofmann (1986). Adding the two polarization components, we obtain

$$\frac{d\mathcal{F}}{d\phi} = \frac{\sqrt{3}}{2\pi} \alpha\gamma \frac{\Delta\omega}{\omega} \frac{1}{e} \frac{\omega}{\omega_c} \int_{\omega/\omega_c}^{\infty} K_{5/3}(y') dy' . \quad (3.19)$$

We remark that this is consistent with Eq. (2.26).

In practical units [photons · s<sup>-1</sup> · mr<sup>-1</sup> · (0.1% bandwidth)<sup>-1</sup>],

$$\frac{d\mathcal{F}}{d\phi} = 2.46 \times 10^{13} E_e [\text{GeV}] I [A] G_1 (\omega/\omega_c) , \quad (3.20)$$

where

$$G_1(y) = y \int_y^\infty K_{5/3}(y') dy' . \quad (3.21)$$

The function  $G_1(y)$  is also plotted in Fig. 3.2. Using Eq. (3.17), we find that  $G_1(\omega/\omega_c)$  vanishes as  $(\omega/\omega_c)^{1/3}$  for  $\omega \ll \omega_c$  and as  $\exp(-\omega/\omega_c)$  for  $\omega \gg \omega_c$ .

Multiplying Eq. (3.19) with  $\hbar\omega$  and integrating over frequencies (replace  $\Delta\omega$  by  $d\omega$ ), we find that  $\omega_c$  is the frequency that divides the spectrum into two parts of equal power.

### 3.3 Angular Divergence

If the angular distribution in  $\psi$  were of Gaussian shape, then the rms divergence  $\sigma_\psi$  can be calculated by taking the ratio of Eq. (3.19) and Eq. (3.12) evaluated at  $\psi = 0$ :

$$\sigma_\psi = \sqrt{\frac{2\pi}{3}} \frac{1}{\gamma} \left( \frac{\omega}{\omega_c} \right)^{-1} \frac{\int_{\omega/\omega_c}^\infty K_{5/3}(y) dy}{K_{2/3}^2(\omega/2\omega_c)} . \quad (3.22)$$

In reality, the distribution is not Gaussian, especially in view of the fact that the distribution for the vertically polarized component vanishes in the horizontal direction  $\psi = 0$ . However,  $\sigma_\psi$  defined by Eq. (3.22) is still a simple and useful measure for the angular divergence. Equation (3.22) is of the form

$$\sigma_\psi = \frac{1}{\gamma} C(\omega/\omega_c) . \quad (3.23)$$

The function  $C(y)$  is plotted in Fig. 3.3. At  $\omega = \omega_c$ ,  $\sigma_\psi \sim 0.64/\gamma$ . The asymptotic behaviors of  $\sigma_\psi$  are, in view of Eq. (3.17),

$$\sigma_\psi \rightarrow \frac{1}{\gamma} \frac{\sqrt{2\pi/3}}{\Gamma(2/3)} \left( \frac{\omega}{\omega_c} \right)^{-1/3} \approx \frac{1.07}{\gamma} \left( \frac{\omega}{\omega_c} \right)^{-1/3} ; \omega \ll \omega_c , \quad (3.24)$$

$$\rightarrow \frac{1}{\gamma} \frac{1}{\sqrt{3}} \left( \frac{\omega}{\omega_c} \right)^{-1/2} \approx \frac{0.58}{\gamma} \left( \frac{\omega}{\omega_c} \right)^{-1/2} ; \omega \gg \omega_c . \quad (3.25)$$

#### 3.3.1 Simple Understanding

Equations (3.24) and (3.25) can be understood in a simple way as follows: Let the synchrotron radiation be emitted with a horizontal angular divergence  $\Delta\phi$ . This means that a segment of the trajectory arc with angular length about  $\Delta\phi$  will contribute to the radiation as illustrated in Fig. 3.4. The transverse dimension of this extended source is

$$\Delta x \sim \rho(\Delta\phi)^2 . \quad (3.26)$$

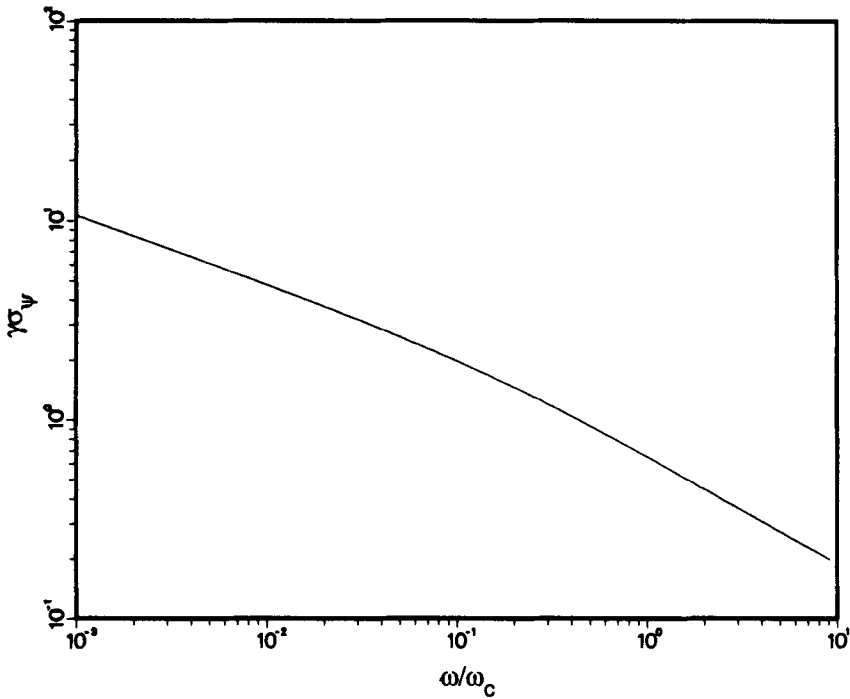


Figure 3.3 The angular spread of bending-magnet radiation times  $\gamma$  as a function of the ratio between the photon frequency and the critical photon frequency  $\omega_c$ .

Now, a radiation field confined transversely will disperse due to diffraction. The diffraction angle must be about  $\Delta\phi$ ,

$$\Delta\phi \sim \frac{\lambda}{\Delta x} \quad , \tag{3.27}$$

where  $\lambda$  is the radiation wavelength. From Eqs. (3.26) and (3.27) we obtain

$$\Delta\phi \sim (\lambda/\rho)^{1/3} \quad , \tag{3.28}$$

$$\Delta x \sim \rho(\lambda/\rho)^{2/3} \quad . \tag{3.29}$$

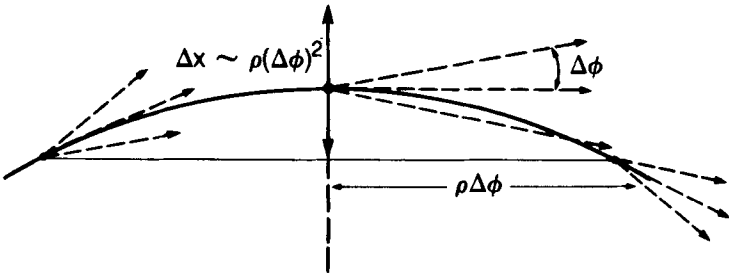


Figure 3.4 Explanation of the angular divergence and the effective transverse size of the bending-magnet radiation.

For the vertical angle  $\Delta\psi$  and size  $\Delta y$ , we have

$$\Delta y \sim \rho \Delta\phi \Delta\psi, \quad (3.30)$$

$$\Delta\psi \sim \lambda / \Delta y. \quad (3.31)$$

From these equations and Eq. (3.28), one finds that

$$\Delta\psi \sim \Delta\phi \sim (\lambda/\rho)^{1/3}, \quad (3.32)$$

$$\Delta y \sim \Delta x \sim \rho(\lambda/\rho)^{2/3}.$$

Equation (3.32) agrees with the low-frequency limit Eq. (3.24). In fact,

$$\Delta\psi \sim \left(\frac{\lambda}{\rho}\right)^{1/3} = \left(\frac{\lambda}{\lambda_c} \frac{\lambda_c}{\rho}\right)^{1/3} = \left(\frac{\omega}{\omega_c}\right)^{-1/3} \left(\frac{\lambda_c}{\rho}\right)^{1/3} \sim \frac{1}{\gamma} \left(\frac{\omega}{\omega_c}\right)^{-1/3}.$$

How do we explain the high-frequency limit [Eq. (3.25)]? In that limit, the opening angle becomes smaller than  $\gamma^{-1}$ . However, it is reasonable to suppose that the angular length of the arc should not be smaller than  $\gamma^{-1}$  in view of the discussion in Subsection 2.3.2. Thus, the transverse dimensions of the source in the high-frequency limit should be

$$\Delta x \sim \rho \gamma^{-1} \Delta\phi,$$

$$\Delta y \sim \rho \gamma^{-1} \Delta\psi. \quad (3.33)$$

The diffraction condition, Eqs. (3.27) and (3.31), remains unchanged. From these we obtain

$$\begin{aligned} \Delta x \sim \Delta y &\sim \sqrt{\frac{\lambda \rho}{\gamma}} \\ \Delta\phi \sim \Delta\psi &\sim \sqrt{\frac{\lambda_c \gamma}{\rho}} \sqrt{\frac{\lambda}{\lambda_c}} \sim \frac{1}{\gamma} \sqrt{\frac{\omega_c}{\omega}}. \end{aligned} \quad (3.34)$$

Equation (3.34) is in accord with Eq. (3.25).

We have introduced the concept of the source size for the synchrotron radiation. This is the size of the image when the radiation is focused by 1:1 optics. These will be discussed in detail in Section 6.

### 3.4 Polarization

The amplitude for the bending-magnet radiation given by Eq. (3.11) has two polarization components, the horizontal component  $A_\sigma$  and the vertical component  $A_\pi$ . The polarization is linear when observed in the horizontal plane  $\psi = 0$ . Out of this plane, the polarization is elliptical as  $A_\sigma$  and  $A_\pi$  are  $90^\circ$  out of phase. The major and the minor axis of the polarization ellipse is in the horizontal and the vertical direction respectively. The ratio of the lengths of the minor to the major axis is

$$\frac{b}{a} = \frac{X K_{1/3}(\eta)}{\sqrt{1 + X^2 K_{2/3}(\eta)}}. \quad (3.35)$$



As the vertical angle  $\psi$  becomes large, the polarization becomes circular asymptotically. The sense of the electric field rotation for the case  $\psi > 0$  is opposite to that for the case  $\psi < 0$ .

The relative magnitudes of the horizontal and the vertical components of the angular density of the flux, Eq. (3.12), are shown in Fig. 3.5 as functions of the emission angle, for different energies. The square root of the ratio of these intensities is the ratio given by Eq. (3.35).

### 3.5 Frequency-Integrated Power

Substituting the bending magnet trajectory into Eq. (2.39), we obtain

$$\left( \frac{d^2 P_\sigma}{d^2 \Omega} \right) = \frac{e^2}{4\pi\epsilon_0} \cdot \frac{\omega_p}{4\pi c} \frac{1}{e} \int_{-\infty}^{\infty} d\xi \frac{1}{\kappa^5} \left( \frac{\frac{1}{4}(\xi^2 - \psi^2 - \gamma^{-2})^2}{\xi^2 \psi^2} \right).$$

In the above, the integration variable is  $\xi = \omega_p t'$ . After carrying out the integral, one obtains

$$\left( \frac{d^2 P_\sigma}{d^2 \Omega} \right) = \frac{d^2 P}{d^2 \Omega} \bigg|_0 \frac{1}{(1 + \gamma^2 \psi^2)^{3/2}} \left( \frac{1}{7} \frac{\gamma^2 \psi^2}{1 + \gamma^2 \psi^2} \right). \quad (3.36)$$

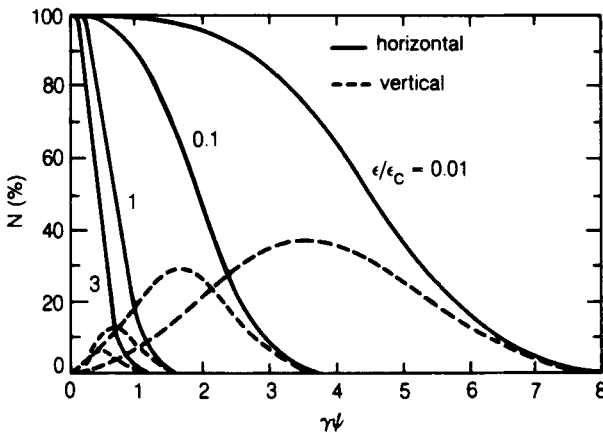


Figure 3.5 Normalized intensities of horizontal and vertical polarization components, as functions of the vertical observation angle  $\psi$ , for different photon energies. (Adapted from Green, 1976)

Here

$$\left. \frac{d^2P}{d^2\Omega} \right|_0 = \frac{7}{64\pi} \frac{e^2}{\epsilon_0} \frac{\gamma^5}{\rho} \frac{I}{e} = \frac{7}{64\pi} \frac{e^2}{\epsilon_0} \frac{eB}{m_e c} \gamma^4 \frac{I}{e} \quad (3.37)$$

is the power density in the forward direction. In the above, we used Eq. (3.1) to convert it into second form. In units of  $W \cdot m^{-2}$ , this becomes

$$\left. \frac{d^2P}{d^2\Omega} \right|_0 = 5.42 \text{ B[T]} E_e^4 [\text{GeV}] I [\text{A}].$$

Integrating Eq. (3.36) over the angles, we obtain

$$\begin{pmatrix} P_\sigma \\ P_\pi \end{pmatrix} = \frac{2}{3} \frac{e^2}{4\pi\epsilon_0} \frac{I}{e} \frac{\gamma^4}{\rho^2} \ell \begin{pmatrix} 7/8 \\ 1/8 \end{pmatrix}. \quad (3.38)$$

Here  $\ell = \rho\Delta\phi$  is the length of the arc. The contribution of the horizontally polarized component to the total power is seven times that from the vertically polarized component. In practical units, the total emitted power is

$$P [\text{kW}] = 1.27 E_e^2 [\text{GeV}] B^2 [\text{T}] I [\text{A}] \ell [\text{m}]. \quad (3.39)$$

## 4 UNDULATOR RADIATION

### 4.1 Electron Orbit and Apparent Motion

We consider a planar undulator for which the magnetic field is in the vertical direction (y-direction) and varies periodically along the z-direction. We assume the field variation to be sinusoidal:

$$B_y = -B_0 \sin(2\pi z/\lambda_u), \quad 0 \leq z \leq N\lambda_u. \quad (4.1)$$

Here  $B_0$  is the peak magnetic field,  $\lambda_u$  is the period length and  $N$  the number of periods. By integrating the equation of motion, the electron's transverse velocity  $c\beta_x$  is found to be

$$\beta_x = \frac{K}{\gamma} \cos(2\pi z/\lambda_u). \quad (4.2)$$

Here

$$K = eB_0\lambda_u/2\pi mc = 0.934 \lambda_u [\text{cm}] B_0 [\text{T}] \quad (4.3)$$

is a dimensionless parameter. The maximum slope of the trajectory is

$$\delta = \frac{K}{\gamma}. \quad (4.4)$$

By an undulator, we usually mean a device for which  $\delta \lesssim \gamma^{-1}$ , as discussed in Subsection 2.3.3. This corresponds to  $K \lesssim 1$ . When  $K$  is large, the device is usually called a wiggler. The radiation characteristics of a wiggler are similar to the bend-

ing magnets. The wiggler limit of the undulator radiation will be discussed in Section 5. Undulators and wigglers operate in the straight sections of storage rings and are collectively known as the insertion devices.

Short-period-length insertion devices producing high magnetic fields are usually constructed from permanent magnets after the pioneering work by Halbach (1983). A typical insertion device, based on a permanent-magnet-steel hybrid design, is illustrated in Fig. 4.1. With optimum design, the peak field strength is given by

$$B_0[\text{T}] = 3.44 \exp \left[ -\frac{g}{\lambda_u} \left( 5.08 - 1.54 \frac{g}{\lambda_u} \right) \right] \quad [\text{neodymium-iron}] \quad ,$$

$$B_0[\text{T}] = 3.33 \exp \left[ -\frac{g}{\lambda_u} \left( 5.47 - 1.8 \frac{g}{\lambda_u} \right) \right] \quad [\text{samarium-cobalt}] \quad ,$$

where  $g$  is the full magnetic gap.

The electron velocity in the  $z$ -direction  $c\beta_z$  is obtained by noting that  $\gamma$  is constant in a magnetic field:

$$\beta_z = \sqrt{1 - \frac{1}{\gamma^2} - \beta_x^2} \approx 1 - \frac{1 + K^2/2}{2\gamma^2} - \frac{K^2}{4\gamma^2} \cos(4\pi z/\lambda_u) \quad . \quad (4.5)$$

The nonoscillating part of  $\beta_z$  is

$$\beta^* = 1 - \frac{1 + K^2/2}{2\gamma^2} = 1 - \frac{1}{2\gamma^{*2}} \quad , \quad (4.6)$$

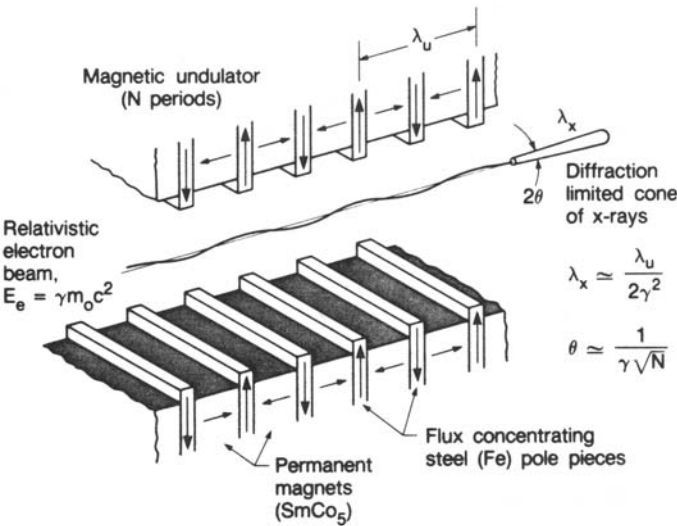


Figure 4.1 Schematic of a periodic magnetic structure (an undulator) of period  $\lambda_u$  and with a number of periods,  $N$ . The structure is based on permanent magnets.

where

$$\gamma^* = \frac{\gamma}{\sqrt{1 + K^2/2}} \quad (4.7)$$

is the  $\gamma$ -factor corresponding to the speed  $c\beta^*$ .

The electron displacements corresponding to Eqs. (4.2) and (4.5) are

$$\frac{1}{c} \mathbf{r}(t') = \left[ \frac{K}{\gamma\omega_u} \sin(\omega_u t'), 0, \left( 1 - \frac{1 + K^2/2}{2\gamma^2} \right) t' - \frac{K^2 \sin(2\omega_u t')}{8\gamma^2\omega_u} \right] \quad (4.8)$$

Here

$$\omega_u = 2\pi c/\lambda_u \quad (4.9)$$

Introducing the coordinate system as shown in Fig. 4.2, we have

$$\mathbf{n} \approx \left[ \varphi, \psi, 1 - \frac{1}{2} \theta^2 \right] \quad (4.10)$$

As before, we assume the angles  $\varphi$  and  $\psi$  are of the order  $\gamma^{-1}$  and have retained only leading terms. The angle  $\theta$  is related to  $\varphi$  (horizontal angle) and  $\psi$  (vertical angle) by

$$\theta^2 = \varphi^2 + \psi^2 \quad (4.11)$$

The observer time given by Eq. (2.17) is

$$t = t' \frac{1 + K^2/2 + \gamma^2\theta^2}{2\gamma^2} + \frac{K^2}{8\omega_u\gamma^2} \sin(2\omega_u t') - \frac{K\varphi}{\omega_u\gamma} \sin(\omega_u t') \quad (4.12)$$

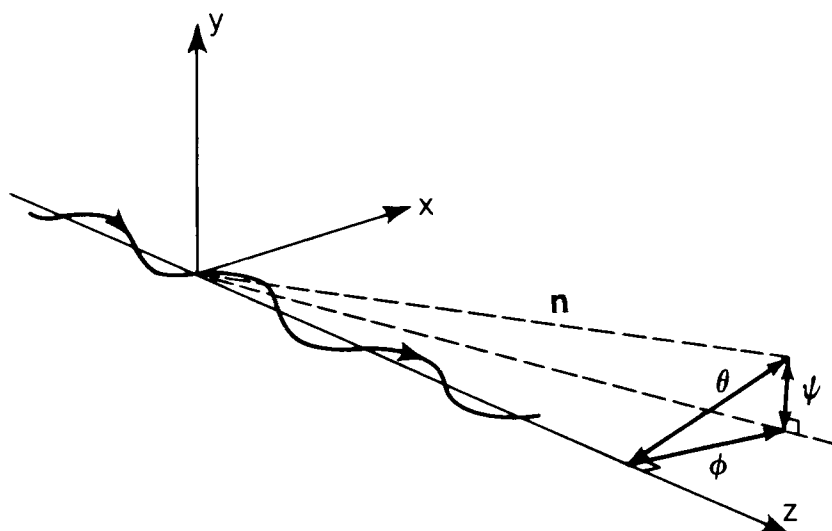


Figure 4.2 Coordinate system for the undulator radiation.

Multiplying both sides of Eq. (4.11) by

$$\omega_1(\theta) = \frac{2\gamma^2}{1 + K^2/2 + \gamma^2\theta^2} \omega_u, \quad (4.13)$$

one obtains

$$\begin{aligned} \omega_1(\theta)t &= \omega_u t' + \frac{K^2}{4(1 + K^2/2 + \gamma^2\theta^2)} \sin(2\omega_u t') \\ &\quad - \frac{2\gamma\phi K}{1 + K^2/2 + \gamma^2\theta^2} \sin(\omega_u t'). \end{aligned} \quad (4.14)$$

The apparent motion is obtained by expressing  $\mathbf{r}(t')$  in terms of  $t$  using Eq. (4.14). From the structure of these equations, it is clear that the apparent motion will be periodic in time with period  $2\pi/\omega_1(\theta)$ . This period is shorter than the period of the electron motion in the emitter time  $2\pi/\omega_u$  by a large factor  $2\gamma^2/(1 + K^2/2 + \gamma^2\theta^2)$ . Thus the undulator radiation will exhibit sharp spectral peaks at frequencies

$$\omega_n(\theta) = n\omega_1(\theta), \quad n = 1, 2, \dots \quad (4.15)$$

Although periodic, the apparent motion is in general not sinusoidal. Figure 4.3 shows the apparent trajectories for one period for different values of  $K$ . For  $K \ll 1$ , the trajectory is almost sinusoidal implying that the higher harmonics are suppressed. As  $K$  increases, the trajectory becomes nonsinusoidal and there will be strong higher harmonics in the spectrum. This is because the time-squeezing becomes nonuniform. For  $K \gg 1$ , the apparent trajectory develops sharp kinks much like in the case of the bending-magnet radiation. This is the so-called wiggler limit, which will be discussed further in Section 5.

The trajectories in Fig. 4.3, although not sinusoidal, have the symmetry that the shape of the trajectory in each half period,  $\ell\pi \leq \omega_1(0)t \leq (\ell + 1)\pi$  for any integer  $\ell$ , is symmetric with respect to the center of the half period. This implies that the Fourier expansion of the trajectory does not contain even harmonics. Thus  $n$  in Eq. (4.15) will only contain odd integers in the forward direction. In the nonforward direction, the points where the slope is parallel to the observation direction are displaced, breaking the above mentioned symmetry. Thus there will in general be radiation at even harmonics. Figure 4.4 shows the apparent trajectories at different observation angles.

We want to point out one more feature of undulator radiation that can be learned by examining the apparent trajectory. The  $x$ -component of  $\mathbf{n} \times (\mathbf{n} \times \mathbf{r})$  appearing in a (Eq. (2.16)) is, assuming  $\psi = 0$  and retaining only the leading terms,

$$\phi z(t') - x(t') \approx c \left[ \phi t' - \frac{K}{\gamma\omega_u} \sin(\omega_u t') \right]. \quad (4.16)$$

Using Eq. (4.14) to rewrite  $t'$  in terms of  $t$ , this becomes

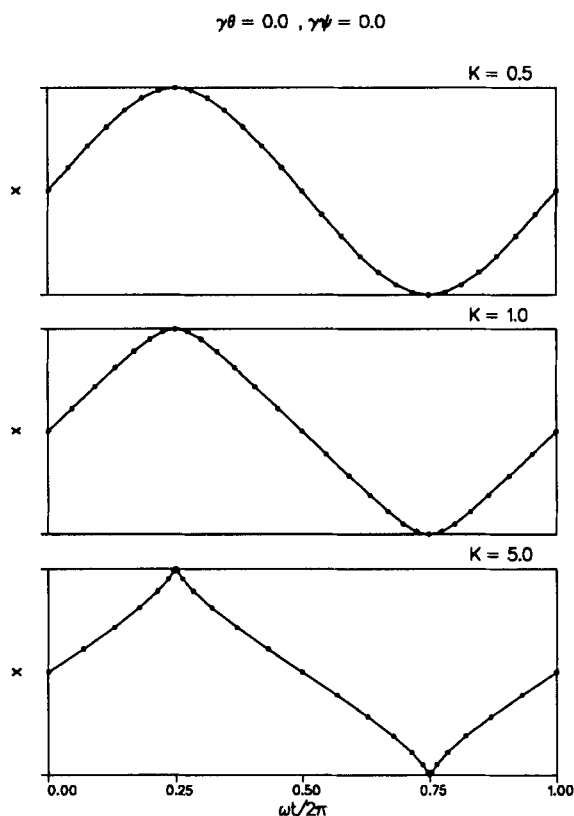


Figure 4.3 The apparent undulator trajectories (one period) in the  $z$ -direction at different values of  $K$ . Notice the sharpening of the trajectory at higher  $K$ , indicating the higher harmonic contents.

$$\frac{c}{\omega_u} \left[ \omega_1(\varphi)\varphi t + \frac{\gamma^2\varphi^2 - 1 - K^2/2}{1 + K^2/2 + \gamma^2\varphi^2} \frac{K}{\gamma} \sin(\omega_u t') - \frac{K^2\varphi}{4(1 + K^2/2 + \gamma^2\varphi^2)} \sin(2\omega_u t') \right] . \quad (4.17)$$

The first term in the above is linear in the observer time  $t$  and does not contribute to an acceleration. The second term will give rise to a sequence of harmonics starting from the fundamental. The third term gives rise to another, generally weaker sequence of harmonics starting from the second harmonic. When

$$\varphi = \sqrt{\frac{1 + K^2/2}{\gamma^2}} = \frac{1}{\gamma^*} , \quad (4.18)$$

the second term vanishes and the radiation intensity will be suppressed. This phenomenon has a simple explanation in the frame moving with the velocity  $c\beta^*$  along the  $z$ -direction [Motz, 1951; Purcell, 1972]: in that frame, the radiation in the

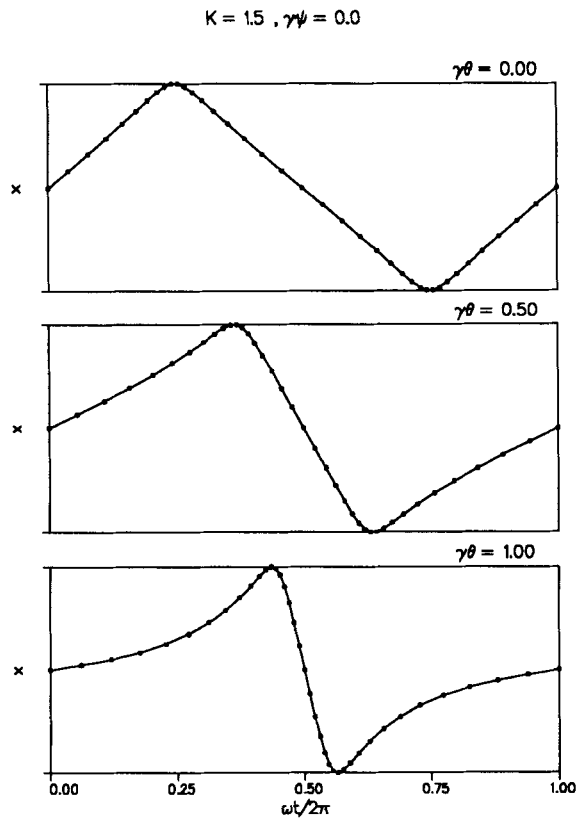


Figure 4.4 The apparent undulator trajectory (one period) observed at different horizontal angle  $\varphi$ . As  $\varphi$  increases, the two points of amplitude extremum move toward each other, breaking the symmetry within each half-period. Thus there will be even harmonics in the spectrum.

x-direction is strongly suppressed because the electron executes dipole oscillation in that direction. The direction (4.18) in the laboratory frame, when Lorentz-transformed to the moving frame, becomes the x-direction in the moving frame.

4.2 Spectral-Angular Characteristics [Alferov, et al., 1973; Kincaid, 1977]

We use Eqs. (2.41) and (2.42), and introduce a more convenient integration variable as follows:

$$\xi = \omega_u t' \quad . \tag{4.19}$$

The exponent in the integrand of Eq. (2.42) becomes, in view of Eq. (4.14),

$$\omega t = \frac{\omega}{\omega_1(\theta)} \xi - p \sin \xi + q \sin 2\xi \quad . \tag{4.20}$$

Here

$$p = 2 \frac{\omega}{\omega_1(0)} \frac{\varphi \gamma K}{1 + K^2/2}, \quad q = \frac{1}{4} \frac{\omega}{\omega_1(0)} \frac{K^2}{1 + K^2/2}. \quad (4.21)$$

Inserting these into Eq. (2.42), one obtains

$$A_{\sigma,\pi} = \frac{\omega \gamma K}{\omega_1(0)(1 + K^2/2)} \frac{\sin \left( N\pi\omega/\omega_1(\theta) \right)}{\sin \left( \pi\omega/\omega_1(\theta) \right)} B_{\sigma,\pi}(\omega, \varphi, \psi), \quad (4.22)$$

where

$$\begin{aligned} \begin{pmatrix} B_{\sigma}(\omega, \varphi, \psi) \\ B_{\pi}(\omega, \varphi, \psi) \end{pmatrix} &= \frac{1}{\pi} \int_{-\pi}^{\pi} d\xi \begin{pmatrix} \varphi/K - \cos \xi \\ \psi/K \end{pmatrix} \\ &\times \exp i \left[ \left( \omega/\omega_1(\theta) \right) \xi - p \sin \xi + q \sin 2\xi \right]. \end{aligned} \quad (4.23)$$

Inserting Eq. (4.23) into Eq. (2.41), we finally obtain

$$\begin{aligned} \frac{d^2 \mathcal{F}_{\sigma,\pi}}{d^2 \Omega} &= \alpha \frac{\Delta \omega}{\omega} \frac{1}{e} \left[ \frac{K \gamma}{1 + K^2/2} \right]^2 \left[ \frac{\omega}{\omega_1(0)} \right]^2 \\ &\times N^2 S_N \left( \omega/\omega_1(\theta) \right) B_{\sigma,\pi}^2(\omega, \varphi, \psi). \end{aligned} \quad (4.24)$$

Here

$$S_N \left( \omega/\omega_1(\theta) \right) = \left[ \frac{\sin N\pi\omega/\omega_1(\theta)}{N \sin \pi\omega/\omega_1(\theta)} \right]^2. \quad (4.25)$$

We now study Eq. (4.24).

#### 4.2.1 Spectrum at a Given Angle

The function  $S_N$  has sharp peaks at frequencies given by Eq. (4.15):

$$\omega = n\omega_1(\theta) = n\omega_1(0) \frac{1}{1 + \gamma^2 \theta^2 / (1 + K^2/2)}. \quad (4.15)$$

Here

$$\omega_1(0) = \frac{2\gamma^2}{1 + K^2/2} \omega_u. \quad (4.26)$$

The photon energy and the wavelength corresponding to  $\omega_1(0)$  in practical units are, respectively,



$$\varepsilon_1 [\text{keV}] = \frac{0.95 E_e^2 [\text{GeV}]}{(1 + K^2/2) \lambda_u [\text{cm}]} ,$$

$$\lambda_1 [\text{\AA}] = \frac{(1 + K^2/2) \lambda_u}{2\gamma^2} = \frac{13.1 \lambda_u [\text{cm}]}{E_e^2 [\text{GeV}]} (1 + K^2/2) . \quad (4.27)$$

The angular dependence of undulator frequencies lies its origin in Lorentz transformation: The  $n$ th harmonic corresponds to a multipole field in the moving frame discussed in connection with Eq. (4.18). Although the frequency of a multipole field is independent of the observation angle, it becomes angle dependent when Lorentz-transformed to the laboratory frame. The angular dependence of the undulator frequencies has been vividly demonstrated by the colorful radiation patterns for undulators in the visible spectral regions (see for example, Synchrotron Radiation News, 1988).

The width of the spectral line (FWHM) near  $n$ th harmonic is

$$\left. \frac{\Delta\omega}{\omega_n} \right|_N = \frac{2.8}{\pi n N} \sim \frac{0.9}{n N} . \quad (4.28)$$

This bandwidth can be understood from the time-domain picture of the undulator radiation: An  $N$ -period undulator produces an  $N$ -cycled wavetrain (the time-squeezed signal), the length of which is

$$\ell_c \sim N \lambda_1 . \quad (4.29)$$

The bandwidth at  $n$ th harmonic is therefore

$$\left. \frac{\Delta\lambda}{\lambda_n} \right|_N \sim \left. \frac{\Delta\omega}{\omega_n} \right|_N \sim \frac{\lambda_n}{\ell_c} \sim \frac{1}{n N} ,$$

in agreement with Eq. (4.28). In the above, the subscript  $N$  is to indicate that the width is due to the  $N$ -period effect. Since  $N$  is typically about 100, the bandwidths of the spectral peaks are about 1% or less. The bandwidth given by Eq. (4.28) is sometimes referred to as the homogeneous bandwidth in analogy with the laser terminology.

In Fig. 4.5, we illustrate the spectral peaks of the undulator radiation by calculating the angular density of the spectral flux, given by Eq. (4.24), as a function of  $\omega/\omega_1(0)$ . The spectrum is calculated at a slightly nonforward direction so that the peaks at even harmonics are visible.

Although the undulators produce sharp spectral peaks, the position of these peaks can be changed either by changing the electron beam energy  $E_e$  or changing the magnetic field, thus changing  $\gamma$  or  $K$  in Eq. (4.26). For permanent-magnet undulators, the change in the magnetic field is accomplished by changing the magnetic gap. The ability to tune the radiation frequency is crucial for many experiments.

#### 4.2.2 Angular Pattern at a Given Frequency and Central Cone

We consider the behavior of  $S_N$  as a function of  $\theta$  for a fixed frequency near  $\omega_n = n\omega_1(0)$ . We write

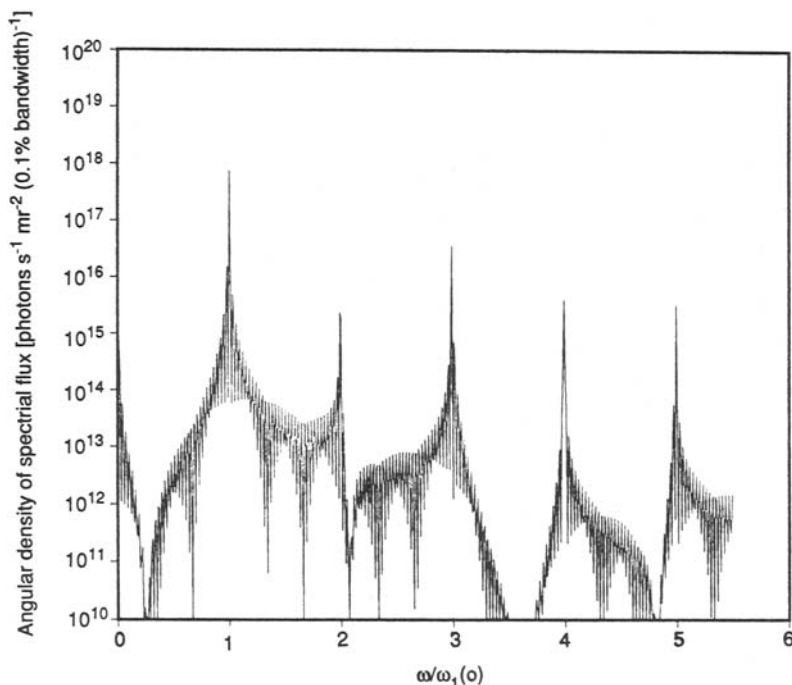


Figure 4.5 The angular density of the spectral flux as a function of the ratio  $\omega/\omega_1(0)$ . The undulator parameters are  $\lambda_u = 3.65$  cm,  $N = 134$  and  $K = 1$ . The electron parameters are  $E_e = 1.5$  GeV,  $I = 0.4$  A and zero emittance. The density is evaluated at a small nonvanishing angle  $\gamma^*\varphi = 0.05$  in order to show the contribution from even harmonics.

$$\frac{\omega}{\omega_1(0)} = n + \Delta\nu \quad . \quad (4.30)$$

For  $\Delta\nu \ll 1$  and  $n\theta^2/(1 + K^2/2) \ll 1$ ,  $S_N$  becomes

$$S_N \sim \left( \frac{\sin N\pi \left[ \Delta\nu + n\theta^2/(1 + K^2/2) \right]}{N\pi \left[ \Delta\nu + n\theta^2/(1 + K^2/2) \right]} \right)^2 \quad . \quad (4.31)$$

Thus the angular distribution has a maximum in the forward direction when  $\Delta\nu \geq 0$ , while it has a dip when  $\Delta\nu < 0$ . At the exact location of the  $n$ th harmonic, i.e.,  $\Delta\nu = 0$ , we approximate Eq. (4.32) by a Gaussian shape:

$$S_N(\Delta\nu = 0, \theta) \sim \exp \left[ -\frac{\theta^2}{2\sigma_r^2} \right] = \exp \left[ -\frac{\varphi^2 + \psi^2}{2\sigma_r^2} \right] \quad . \quad (4.32)$$

We fix  $\sigma_r$  by requiring that the two expressions, Eqs. (4.31) and (4.32), give the same results when integrated over the solid angle. One obtains

$$\sigma_r = \frac{1}{2\gamma} \sqrt{\frac{1 + K^2/2}{nN}} = \sqrt{\frac{\lambda_n}{2L}} \quad (4.33)$$

where  $\lambda_n = \lambda_1/n$  is the wavelength corresponding to  $\omega_n$  and  $L = N\lambda_u$  is the length of the undulator.  $\sigma_r$  is smaller by about a factor  $\sqrt{nN}$  compared to the typical opening angle  $\gamma^{-1}$  of the bending magnet radiation. For  $L = 5\text{m}$  and  $\lambda_n = 100\text{Å}$ ,  $\sigma_r \sim 30\text{ }\mu\text{rad}$ . The region around the central peak of the angular distribution will be referred to as the *central cone*. The useful flux of undulator section is mainly contained in the narrow central cone.

In the previous subsection, we have considered the width of the spectral line  $\Delta\omega/\omega|_N$  due to the finite number of oscillation periods  $N$ . There is an additional broadening due to the angular effect arising from the angle dependence of the undulator frequency, Eq. (4.15). When the radiation is observed through an angular aperture  $\Delta\theta$ , the additional broadening is

$$\left. \frac{\Delta\omega}{\omega} \right|_{\Delta\theta} \sim \frac{\gamma^2 \Delta\theta^2}{1 + K^2/2} \quad (4.34)$$

For  $\Delta\theta \sim \sigma_r$ ,  $\Delta\omega/\omega|_{\Delta\theta}$  becomes about  $\Delta\omega/\omega|_N$ . Thus the rms angular size of the central cone can be considered as an optimum half-width of the angular aperture to accept undulator radiation; at smaller aperture the flux is sacrificed while at larger aperture the spectrum of the transmitted photons lies in large part outside the minimum possible bandwidth  $\Delta\omega/\omega|_N$ .

Photons are also emitted into discrete annular regions around the central cone at angles  $\theta_{n\ell}$ ,  $\ell = 1, 2, \dots$ . These photons belong to the higher harmonic  $n' = n + \ell$ , but their frequency becomes the same as the central cone frequency  $\omega_n = \omega_1(0)$  because they are observed at larger angles. The angle  $\theta_{n\ell}$  is determined by

$$n\omega_1(0) = (n + \ell)\omega_1(\theta_{n\ell}) \quad .$$

This gives

$$\theta_{n\ell} = \frac{1}{\gamma} \sqrt{\frac{\ell}{n} (1 + K^2/2)} \quad (4.35)$$

The width of the annular region  $\Delta\theta_{n\ell}$  determined from the function  $S_N$  is about

$$\Delta\theta_{n,\ell} \sim \frac{\lambda_n}{\theta_{n,\ell} L} \quad (4.36)$$

This width is smaller than  $\sigma_r$  roughly by a factor  $\sqrt{N}$ .

Figure 4.6 shows an example of the angular distribution of undulator radiation calculated from Eq. (4.24) to illustrate the central cone and annular regions.

We close this subsection by giving a simple derivation of the angular widths  $\sigma_r$  (Eq. (4.33)) and  $\Delta\theta_{n,\ell}$  (Eq. (4.36)) using arguments similar to the case of the bending magnet in Subsection 3.3.1: Let  $\Delta\theta$  be the angular spread of the radiation from an undulator of length  $L$ . If the radiation is observed near the forward direction, the transverse size will be

$$\Delta x \sim L\Delta\theta \quad (4.37)$$

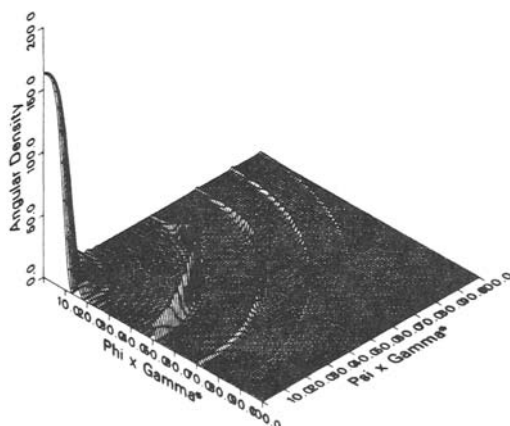


Figure 4.6 An illustration of the angular distribution of undulator radiation at  $\omega = \omega_1(0)$  for zero beam emittance. The x and y axes are  $\gamma^*\varphi$  and  $\gamma^*\psi$ , respectively. The undulator parameters are  $N = 15$  and  $K = 1$ .

An electromagnetic field confined transversely will spread out due to diffraction, and the diffraction angle should be about  $\Delta\theta$  by self-consistency:

$$\Delta\theta \sim \frac{\lambda}{\Delta x} . \quad (4.38)$$

Combining (4.37) and (4.38), we obtain

$$\Delta x \sim \sqrt{\lambda L} \quad (4.39)$$

$$\Delta\theta \sim \sqrt{\frac{\lambda}{L}} . \quad (4.40)$$

We see that  $\Delta\theta$  given by Eq. (4.40) is the same as  $\sigma_r$  within a factor of  $\sqrt{2}$ .

If the radiation is observed away from the forward direction at an angle  $\theta \gg \Delta\theta$ , then the transverse size will be given by, instead of Eq. (4.37),

$$\Delta x \sim \theta \cdot L . \quad (4.41)$$

The diffraction angle corresponding to this is  $\lambda/\Delta x$ , which reproduces Eq. (4.36).

### 4.2.3 The Peak Angular Density and the Flux in the Central Cone

To obtain the angular density at the peak of the central cone, we evaluate Eq. (4.23) in the forward direction  $\varphi = \psi = 0$ . The  $\pi$ -component vanishes, and

$$B_\sigma(\omega_n, 0, 0) = \frac{-1}{\pi} \int_{-\pi}^{\pi} \cos \xi \exp \left[ i(n\xi + q \sin 2\xi) \right] . \quad (4.42)$$

The integral vanishes for even harmonics. For an odd integer  $n$ , the integral can be expressed in terms of the Bessel functions  $J_s$  as follows:

$$B_{\sigma}(\omega_n, 0, 0) = (-1)^{\frac{n+1}{2}} \left[ J_{\frac{n-1}{2}}(q) - J_{\frac{n+1}{2}}(q) \right], \quad n = \text{odd integers} \quad (4.43)$$

Inserting this into Eq. (4.24), we obtain the peak angular density at  $n$ th harmonic

$$\begin{aligned} \left. \frac{d^2 \mathcal{F}^n}{d^2 \Omega} \right|_0 &= \left. \frac{d^2 \mathcal{F}_{\sigma}^n}{d^2 \Omega} \right|_0 = \alpha N^2 \gamma^2 \frac{\Delta \omega}{\omega} \frac{I}{e} F_n(K) \quad (n = 1, 3, 5, \dots) \\ &= 0 \quad (n = 2, 4, 6, \dots), \end{aligned} \quad (4.44)$$

where

$$F_n(K) = \frac{K^2 n^2}{(1 + K^2/2)^2} \left\{ J_{\frac{n-1}{2}} \left[ \frac{nK^2}{4(1 + K^2/2)} \right] - J_{\frac{n+1}{2}} \left[ \frac{nK^2}{4(1 + K^2/2)} \right] \right\}^2. \quad (4.45)$$

In practical units [photons  $\cdot$  s $^{-1} \cdot$  mr $^{-1} \cdot$  (0.1% bandwidth) $^{-1}$ ], Eq. (4.44) becomes

$$\left. \frac{d^2 \mathcal{F}^n}{d^2 \Omega} \right|_0 = 1.74 \times 10^{14} N^2 E_e^2 [\text{GeV}] I [\text{A}] F_n(K).$$

The absence of the even harmonic in the forward direction was discussed in Subsection 4.1. The function  $F_n(K)$  is plotted in Fig. 4.7, showing that the higher harmonics become more prominent as  $K$  becomes large. This was also discussed in Subsection 4.1. See in particular Fig. 4.3.

The flux contained in the central cone,  $\mathcal{F}_n$ , is obtained by integrating Eq. (4.24) over the solid angle. Since the  $N$ -dependent factor  $S_N$  is approximated by the Gaussian shape, Eq. (4.32), we have

$$\mathcal{F}^n = \left. \frac{d^2 \mathcal{F}^n}{d^2 \Omega} \right|_0 \cdot 2\pi \sigma_r^2.$$

Using Eq. (4.33), this becomes

$$\mathcal{F}^n = \frac{\pi}{2} \alpha N \frac{\Delta \omega}{\omega} \frac{I}{e} Q_n(K), \quad (4.46)$$

where

$$Q_n(K) = (1 + K^2/2) F_n(K) / n. \quad (4.47)$$

The function  $Q_n(K)$  is plotted in Fig. 4.8. In practical units [photons  $\cdot$  s $^{-1} \cdot$  (0.1% bandwidth) $^{-1}$ ], Eq. (4.46) becomes

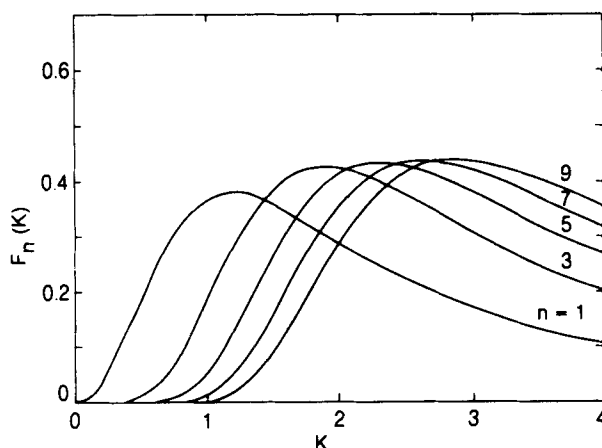


Figure 4.7 The function  $F_n(K)$  for different values of  $n$ , where  $K$  is the deflection parameter.

$$\mathcal{F}^n = \frac{1}{2} \cdot 1.43 \times 10^{14} N Q_n I[A] \quad .$$

The flux formula in the above is one half of those quoted in the previous publications [Krinsky, 1983; Kim, 1986c]. This is because we have computed the flux at  $\omega = n\omega_1(0)$ ; more flux is produced at slightly lower frequencies, and it becomes twice that given by Eq. (4.46) at around  $\omega = \omega_1(0) (n - N^{-1})$ . For these frequencies, however, the angular distribution has a dip in the forward direction, and

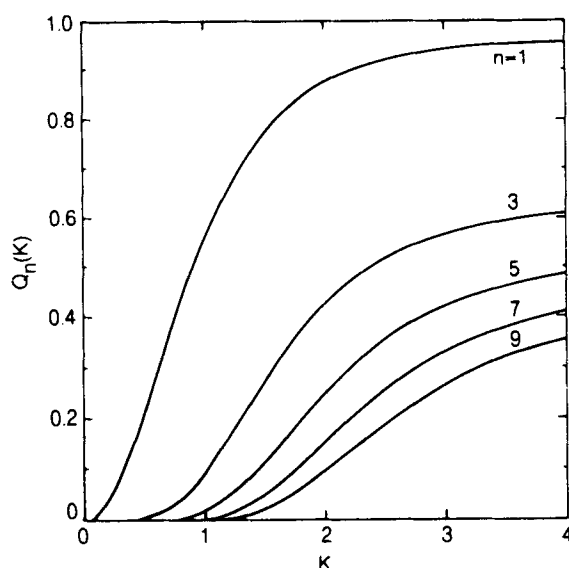


Figure 4.8 The function  $Q_n(K)$  for different values of  $n$ .

therefore the Gaussian approximation used in the present treatment does not apply.

#### 4.2.4 Effect of Electrons' Angular Divergence

So far, we have assumed that all electrons are parallel. However, electrons in a storage ring are distributed in angles. The probability distribution function  $g(\phi, \psi)$  is of Gaussian shape, with rms width  $\sigma_{x'}$  in the horizontal direction and  $\sigma_{y'}$  in the vertical direction. We assume that

$$\sigma_{x'}, \sigma_{y'} \ll \gamma^{-1} . \quad (4.48)$$

In that case, the effects of electrons' angular divergence on bending magnet radiation is small. However, the effects on undulator radiation could be significant.

The effect of the electrons' angular distribution on the peak angular density can be calculated from the relation

$$\left. \frac{d^2 \mathcal{F}}{d^2 \Omega} \right|_0 = \int \frac{d^2 \mathcal{F}^0(\phi, \psi)}{d^2 \Omega} g(\phi, \psi) d\phi d\psi . \quad (4.49)$$

Here  $d^2 \mathcal{F}^0/d^2 \Omega$  is the angular density assuming that all electrons are parallel, and  $g(\phi, \psi)$  is the probability distribution function for the electrons. Equation (4.48), which is intuitively plausible, will be derived in Subsection 6.4. The dominant angular variation in  $d^2 \mathcal{F}^0/d^2 \Omega$  comes from the factor  $S_N$  in Eq. (4.24) which is approximated by the Gaussian shape, Eq. (4.32).

For odd harmonics, the effect can be described by increased widths of the central cone. Since  $S_N$  and  $g$  are both Gaussian, the increased widths in the  $x$ - and the  $y$ -directions are, respectively,

$$\begin{aligned} \sigma_{Tx'} &= \sqrt{\sigma_T^2 + \sigma_{x'}^2} \\ \sigma_{Ty'} &= \sqrt{\sigma_T^2 + \sigma_{y'}^2} . \end{aligned} \quad (4.50)$$

The total flux in the central cone remains unchanged, being given by Eq. (4.46). Thus, the peak angular density taking into account the electron beam distribution is

$$\left. \frac{d^2 \mathcal{F}^n}{d^2 \Omega} \right|_0 = \frac{\mathcal{F}^n}{2\pi \sigma_{Tx'} \sigma_{Ty'}} . \quad (4.51)$$

For even harmonics, we evaluate the function  $B_{\sigma, \pi}$ , Eq. (4.23), at small but nonvanishing angles. Since  $p$  given by Eq. (4.21) is proportional to  $\phi$  and hence small, we expand the integrand to obtain

$$\left( \frac{B_\sigma}{B_\pi} \right) = \frac{1}{\pi} \int_{-\pi}^{\pi} d\xi \left[ \frac{\phi \gamma / K - \cos \xi}{\psi \gamma / K} \right] \left[ 1 - i \frac{2n\phi \gamma K}{1 + K^2/2} \sin \xi \right] \exp i(n\xi + q \sin 2\xi) .$$

This becomes, for even  $n$ ,

$$\begin{pmatrix} B_\sigma \\ B_\pi \end{pmatrix} = 2 \left( \frac{\gamma}{K} \right) (-1)^{n/2} \begin{pmatrix} \varphi \left[ J_{\frac{n}{2}}(q) - 2q \left[ J_{\frac{n+2}{2}}(q) - J_{\frac{n-2}{2}}(q) \right] \right] \\ \psi J_{\frac{n}{2}}(q) \end{pmatrix}.$$

We insert this in Eq. (4.24) to obtain the angular density at small angles. To take into account the electron beam effect, we carry out the integration in Eq. (4.49). In doing this integral, the variation in angles of the factor  $S_N$  must be included. The result is

$$\begin{aligned} \left. \frac{d^2 \mathcal{F}^n}{d^2 \Omega} \right|_0 &= \alpha N \frac{\Delta \omega}{\omega} \frac{1}{e} \frac{n}{1 + K^2/2} \\ &\times \left\{ \frac{\sigma_x^2}{\sigma_r^2 + \sigma_x^2} \left[ J_{\frac{n}{2}}(q) - 2q \left[ J_{\frac{n+2}{2}}(q) - J_{\frac{n-2}{2}}(q) \right] \right]^2 \right. \\ &\quad \left. + \frac{\sigma_y^2}{\sigma_r^2 + \sigma_y^2} J_{\frac{n}{2}}^2(q) \right\}. \end{aligned} \quad (4.52)$$

Here  $q = nK^2/4(1 + K^2/2)$ . The angular densities at even harmonics are smaller by about a factor  $1/(\gamma^2 \sigma_x^2)$  than those at odd harmonics.

#### 4.2.5 The Spectrum of the Angle-Integrated Flux

In this and the next subsections, we study the global behavior of the flux distribution determined by the last factor in Eq. (4.24). We assume that  $N$  is large so that

$$S_N \left( \omega/\omega_1(\theta) \right) \rightarrow \frac{1}{N} \sum_{n=1}^{\infty} \delta \left[ \frac{\omega}{\omega_1(0)} \left[ 1 + \frac{\gamma^2 \theta^2}{1 + K^2/2} \right] - n \right]. \quad (4.53)$$

We integrate Eq. (4.24) over the angles by using the polar coordinates:

$$\varphi = \theta \cos u, \quad \psi = \theta \sin u. \quad (4.54)$$

The result is nonvanishing only for  $\omega \leq n\omega_1(0)$  and one obtains

$$\begin{aligned} \left( \frac{\mathcal{F}_\sigma^n(\omega)}{\mathcal{F}_\pi^n(\omega)} \right) &= \alpha N \frac{\Delta \omega}{2\omega_1(0)} \frac{1}{e} \frac{K^2}{(1 + K^2/2)} \int_{-\pi}^{\pi} du \\ &\times \left| \frac{1}{\pi} \int_{-\pi}^{\pi} d\xi \left[ \frac{\gamma \theta \cos u/K - \cos \xi}{\gamma \theta \sin u/K} \right] \exp i(n\xi - p \sin \xi + q \sin 2\xi) \right|^2. \end{aligned} \quad (4.55)$$



Here

$$\theta = \sqrt{\frac{1 + K^2/2}{\gamma^2} \left( \frac{n\omega_1(0)}{\omega} - 1 \right)} \quad (4.56)$$

and  $p$  and  $q$  are obtained by inserting Eq. (4.54) into Eq. (4.21).

The shape of the function  $\mathcal{F}^n(\omega)$  can be computed numerically and is plotted in Fig. 4.9. Note that, although the angle-integrated spectrum has peaks at odd harmonics of  $\omega_1(0)$ , the spectral widths are broad,  $\Delta\omega/\omega$  being of order unity. This is in contrast to the spectrum observed through a narrow aperture discussed in Subsection 4.2.1.

For  $n = 1$  and  $K \lesssim 1$ , one expands

$$\exp i \left( n\xi - p \sin\xi + q \sin 2\xi \right) = e^{i\xi} \left( 1 - ip \sin\xi + O(K^2) \right) .$$

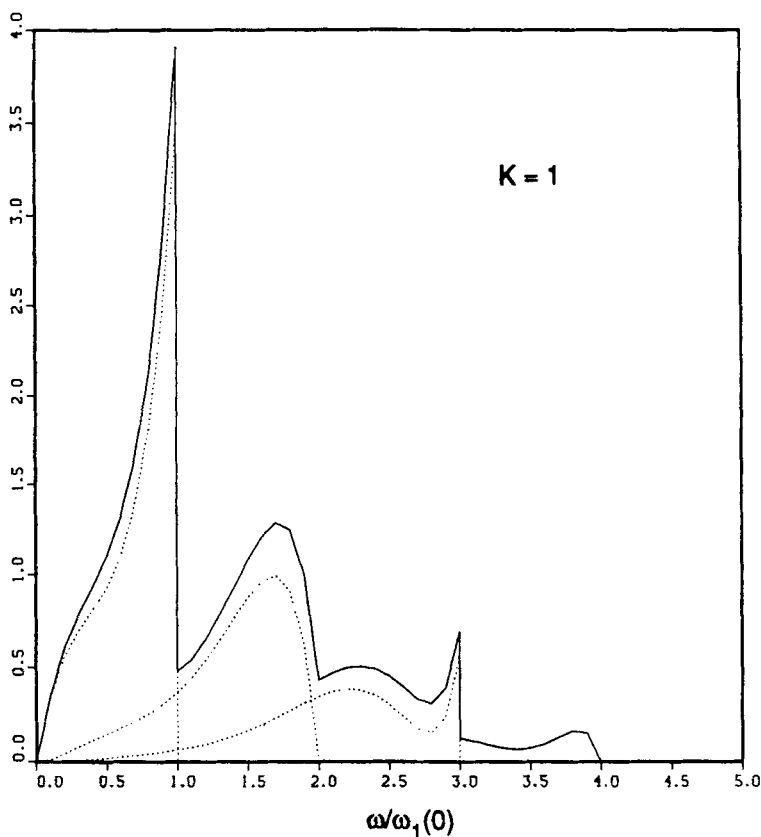


Figure 4.9 The angle-integrated undulator spectrum for  $K = 1$ . The dotted lines are individual harmonics and the solid line is their sum, including up to the 4th harmonic.

Neglecting  $O(K^2)$  terms in the above, the integral in Eq. (4.55) can be done explicitly with the result

$$\mathcal{F}_{\sigma}^1(\omega) = \pi \alpha N \frac{\Delta \omega}{\omega} \frac{1}{e} \frac{K^2}{(1 + K^2/2)} \left[ \frac{\omega}{\omega_1(0)} \right] \left\{ \left[ \frac{\omega}{\omega_1(0)} \right]^2 + \frac{1}{2} \left[ 1 - \frac{\omega}{\omega_1(0)} \right]^2 \right\}; \omega \leq \omega_1(0) \quad (4.57)$$

Similar expansions for  $n > 1$  and other polarization components are worked out by Hofmann (1986).

#### 4.2.6 The Angular Distribution of the Frequency-Integrated Flux

We now integrate Eq. (4.24) with respect to the frequency, and obtain, in view of (4.53),

$$\frac{d^2 \mathcal{F}_{\sigma,\pi}^n}{d^2 \Omega} = \alpha \frac{1}{e} \frac{K^2 \gamma^2 n N}{\left[ 1 + K^2/2 + \gamma^2 \theta^2 \right]^2} B_{\sigma,\pi}(n\omega_1(\theta), \varphi, \psi) \quad (4.58)$$

The function  $B_{\sigma,\pi}$  is easily evaluated numerically. The resulting angular distributions for different  $n$  and different polarization components are shown in Fig. 4.10. Hofmann (1986) has derived approximate expressions for these distributions, which agree very well with the results of exact calculations. Notice that, once integrated over frequencies, the width of the angular distribution becomes about  $1/\gamma$  rather than  $1/\gamma\sqrt{N}$ .

#### 4.3 Polarization

We saw that the bending-magnet radiation is elliptically polarized when observed at some angle away from the bending plane. For radiation from planar undulators, the polarization is always linear. This follows from the fact that the  $\sigma$ - and  $\pi$ -components of the complex amplitude calculated from Eq. (4.23) are relatively real. However, polarization direction, which is in the  $x$ -direction when observed from the horizontal plane, rotates in a complicated way at other directions [Kitamura, 1980].

The linear polarization of the undulator radiation is due to the symmetry of the electron trajectory within each period. Consider the electron trajectory given by Eq. (4.2). When viewed from an angle  $\psi > 0$ , the electron rotates counter clockwise within each half-period,  $2m\pi \leq \omega_u t' \leq (2m+1)\pi$ ,  $m = 1, 2$ , giving rise to elliptically polarized radiation. The electron rotation in the adjacent half-period is in the opposite direction, giving rise to elliptically polarized radiation with the electric field rotating in the opposite direction. As the motions in adjacent half periods are otherwise symmetric, the combined radiation from each full period becomes linearly polarized.

The argument in the above suggests a method to design a planar undulator that produces elliptically polarized radiation in the direction  $\psi \neq 0$ . The idea is to arrange an electron trajectory that is periodic but in which the symmetry within

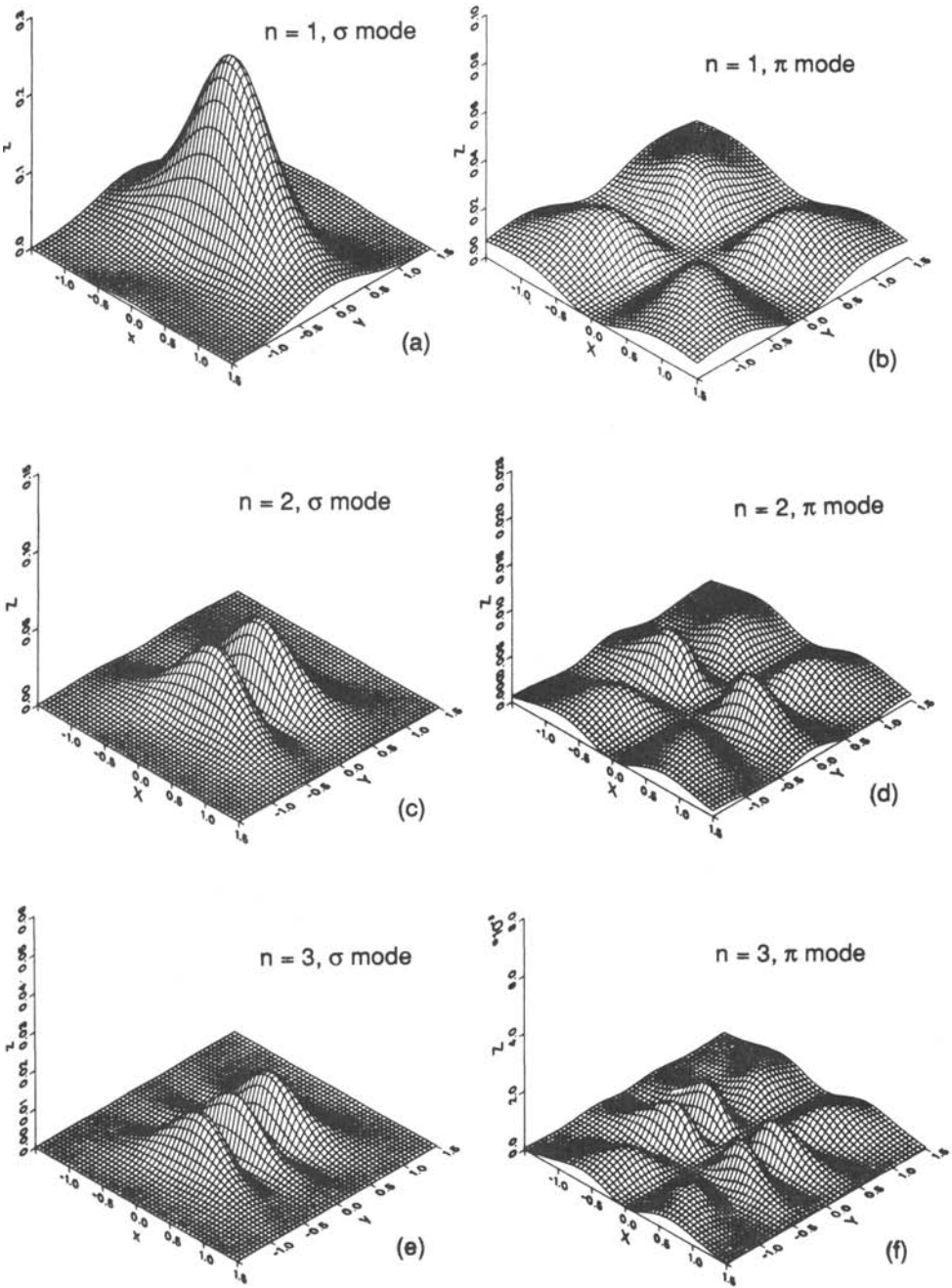


Figure 4.10 The angular distribution of the frequency-integrated flux for  $K = 1$ .

each period is broken. A periodic magnetic field such as the one shown in Fig. 4.11 will produce such a trajectory. In addition to producing elliptically polarized radiation in the direction  $\psi \neq 0$ , it will also produce nonvanishing even harmonics in the forward direction in view of the discussion in Subsection 4.1. It turns out, however, that neither the strength of the on-axis even harmonics nor the deviation from the linear polarization for the off-axis radiation are significant unless the asymmetry is extreme. Such a device was first proposed as a wiggler to produce elliptical polarization [Goulon, et al., 1987]. In a wiggler, the orbit deflection is large and thus the asymmetry could be made large.

### 4.3.1 Special Undulators for Polarization Control

Planar undulators, which we have considered so far and in which all the pole faces are parallel, produce radiation with a high degree of linear polarization. Other kinds of polarized radiation can be obtained by using different magnet arrangements.

**4.3.1.1 Helical Undulator.** Helical undulators produce circularly polarized radiation [Alferov et al., 1974; Kincaid, 1977]. A permanent-magnet helical undulator consists of short segments of dipole magnets, each of which is rotated by a fixed angle  $\Delta\alpha$  relative to the previous one [Halbach, 1981]. Although rather elaborate, it should be possible to design a permanent-magnet helical undulator of variable  $\Delta\alpha$ , and hence of variable period. Such an undulator would be a promising source of circularly polarized radiation, tunable over a wide range of photon energies. The sense of the polarization from the helical undulator described above cannot be reversed while the undulator is operating in a storage ring, because the magnetic field becomes uniform at certain moment and the electron beam will be lost.

**4.3.1.2 Crossed Undulator.** For a variable-polarization capability, one can use a pair of planar undulators oriented at right angles to each other [Moishev, et al., 1978; Kim, 1984], as shown in Fig. 4.12. The amplitude of the radiation from these so-called crossed undulators is a linear superposition of two parts, one linearly polarized along the  $x$  direction and another linearly polarized along the  $y$  direction. By varying the relative phase of the two amplitudes by means of a

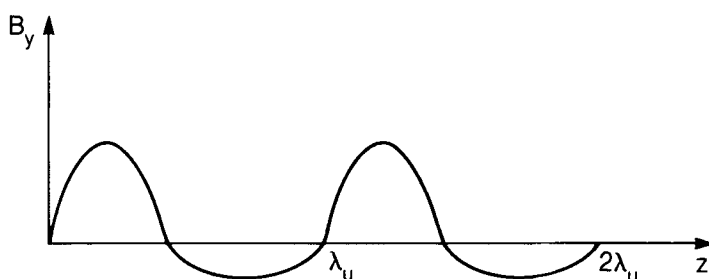


Figure 4.11 Schematic of magnetic field configuration for a nonsinusoidal undulator that can produce even harmonics radiation in the  $z$ -direction and elliptical polarization in directions  $\psi \neq 0$ .

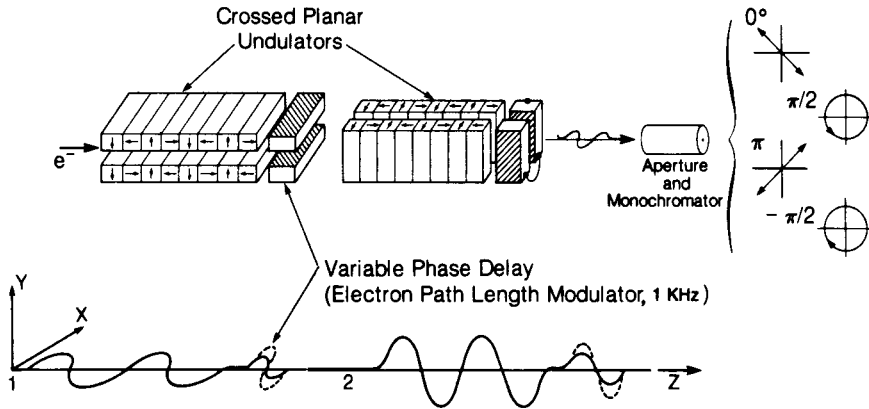


Figure 4.12 Schematic of a pair of crossed undulators, which could be used to produce variably polarized radiation.

variable-field magnet between the undulators, it is possible to modulate the polarization in an arbitrary way: The polarization can be linear and switched between two mutually perpendicular directions, or it can be switched between left circular and right circular. For this device to work, it is necessary to use a monochromator with a sufficiently small bandpass, so that the wave trains from the two undulators are stretched and overlapped. Also, the angular divergence of the electron beam should be sufficiently small; otherwise, the fluctuation in the relative phase limits the achievable degree of polarization. An arrangement of two helical coils producing variable polarization was described by Alferov, et al. (1976).

**4.3.1.3 Other Devices.** A planar undulator whose pole boundaries are tilted away from a right angle with respect to the axial direction can be used as a helical undulator if the electron trajectory lies a certain distance above or below the horizontal mid-plane of the undulator [Halbach, 1985]. Also, Onuki (1986) has proposed a different type of the crossed undulators in which the two orthogonal undulators overlap in the axial direction, producing a helical field. The device has been built and tested; polarization has been observed in good agreement with theory [Onuki et al., 1988].

#### 4.4 Frequency-Integrated Power [Kim, 1986a]

Inserting the undulator trajectory equations to Eq. (2.39), one obtains

$$\left( \frac{d^2 P_\sigma}{d^2 \Omega} \right) = N \frac{e^2}{2\pi\epsilon_0 c} \gamma^4 K^2 \omega_u \frac{I}{e} \left[ \frac{1}{\pi} \int_{-\pi}^{\pi} d\xi \frac{\sin^2 \xi}{D^5} \left[ \left( \frac{1 + X^2 - Y^2}{4X^2 Y^2} \right)^2 \right] \right], \quad (4.59)$$

where

$$\begin{aligned} X &= \gamma\psi \\ Y &= K \cos \xi - \varphi\gamma \\ D &= 1 + X^2 + Y^2 \end{aligned}$$

In the forward direction, the  $\pi$ -component vanishes and the  $\sigma$ -component of the integral within the square brackets in Eq. (4.59) becomes

$$\frac{1}{\pi} \int_{-\pi}^{\pi} d\xi \sin^2 \xi \frac{(1 - K^2 \cos^2 \xi)^2}{(1 + K^2 \cos^2 \xi)^5} = \frac{7}{16 K} G(K) \quad .$$

Here

$$G(K) = \frac{K \left[ K^6 + \frac{24}{7} K^4 + 4K^2 + \frac{16}{7} \right]}{(1 + K^2)^{7/2}} \quad . \quad (4.60)$$

Thus, we can write

$$\frac{d^2 P}{d^2 \Omega} = \frac{d^2 P_{\sigma}}{d^2 \Omega} + \frac{d^2 P_{\pi}}{d^2 \Omega} = \frac{d^2 P}{d^2 \Omega} \bigg|_0 \cdot f_K(\gamma\varphi, \gamma\psi) \quad . \quad (4.61)$$

Here

$$f_K(\gamma\varphi, \gamma\psi) = \frac{16K}{7\pi G(K)} \int_{-\pi}^{\pi} d\xi \frac{\sin^2 \xi}{D^5} \left[ (1 + X^2 - Y^2)^2 + 4X^2 Y^2 \right] \quad (4.62)$$

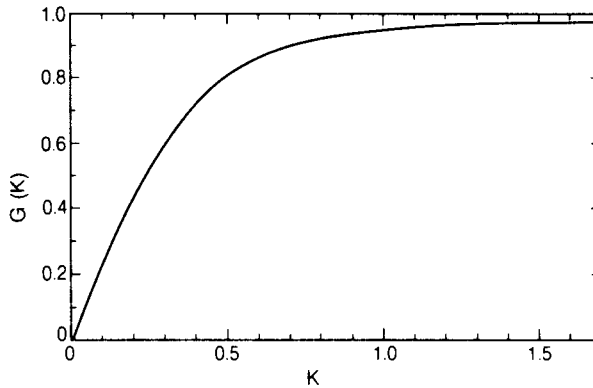
is a function describing the angular dependence normalized so that  $f_K(0,0) = 1$ . The power density in the forward direction is

$$\frac{d^2 P}{d^2 \Omega} \bigg|_0 = \left\{ \frac{7}{64\pi} \frac{e^2}{\epsilon_0 c} \gamma^4 K \omega_u \frac{I}{e} \right\} 2NG(K) \quad . \quad (4.63)$$

Using the definition of  $K$ , Eq. (4.3), we find that the expression within the curly brackets in the above is the same as the peak power density for the bending magnet, Eq. (3.37), if one replaces the bending field  $B$  by the peak undulator field  $B_0$ . The factor  $2N$  accounts for the  $2N$  poles in an  $N$ -period undulator, and the factor  $G(K)$  accounts for the interference effect. The function  $G(K)$  is plotted in Fig. 4.13. From the plot, we see that the power density in the forward direction is less than that expected from a sequence of bending magnets. However,  $G(K)$  is practically unity for  $K \gtrsim 1$ . In practical units of  $W \cdot \text{mr}^{-2}$ , Eq. (4.63) becomes

$$\frac{d^2 P}{d^2 \Omega} \bigg|_0 \left[ W \cdot \text{mr}^{-2} \right] = 10.84 B_0 [T] E^4 [\text{GeV}] I [A] NG(K) \quad .$$

When  $K \rightarrow \infty$ , Eq. (4.62) becomes

Figure 4.13 The function  $G(K)$ .

$$K \rightarrow \infty : f_K(\gamma\phi, \gamma\psi) = \sqrt{1 - (\gamma\phi/K)^2} \times \left\{ \frac{1}{\left[1 + (\gamma\psi)^2\right]^{5/2}} + \frac{5(\gamma\psi)^2}{7 \left[1 + (\gamma\psi)^2\right]^{7/2}} \right\}. \quad (4.64)$$

The factor within the curly brackets is the same as the angular distribution of the power from bending magnets, given by Eq. (3.36), while the factor  $\sqrt{1 - (\gamma\phi/K)^2}$  arises because the magnetic field observed in the  $\phi$  direction in a sinusoidal trajectory is reduced by that factor. In the limit  $K \rightarrow 0$ , one can derive from Eq. (4.62) that

$$K \rightarrow 0 : f_K(\gamma\phi, \gamma\psi) = \frac{1 + 2\gamma^2(\psi^2 - \phi^2) + \left[\gamma^2(\phi^2 + \psi^2)\right]^2}{\left[1 + \gamma^2(\phi^2 + \psi^2)\right]^5}. \quad (4.65)$$

This expression was first derived by Hofmann (1978). Also see Fig. 4.14.

Integrating Eq. (4.59) over the solid angle, we find that the power contained in the  $\sigma$ -polarization is seven times that in the  $\pi$ -polarization as was the case for the bending-magnet radiation. The total power is given by

$$P = \frac{N}{6} \frac{e^2}{\epsilon_0 c} \frac{1}{e} \omega_u \gamma^2 K^2 = \frac{e^2}{12\pi\epsilon_0} \left( \frac{eB_0}{mc} \right)^2 \gamma^2 L \frac{1}{e}. \quad (4.66)$$

This can be obtained from Eq. (3.38) by replacing  $\ell \rightarrow L$  and  $B^2 \rightarrow (1/2) B_0^2$ . The factor 1/2 here accounts for the fact that the magnetic field is not constant but sinusoidal. In practical units, Eq. (4.66) becomes

$$P [\text{kW}] = 6.4 E_e^2 [\text{GeV}] B_0^2 [\text{T}] I [\text{A}] L [\text{m}].$$

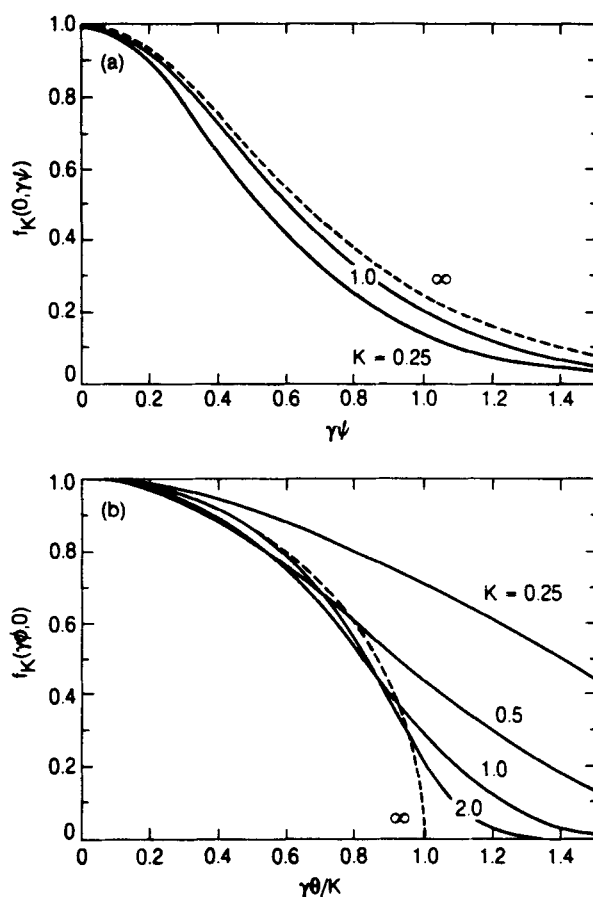


Figure 4.14 The angular distribution of the frequency-integrated power for different values of  $K$ , as a function of the vertical observation angle  $\psi$  when the horizontal observation angle  $\phi = 0$  (a), and as a function of  $\phi$  when  $\psi = 0$  (b).

## 5 THE WIGGLER AS A LARGE $K$ LIMIT OF AN UNDULATOR

When  $K \lesssim 1$ , the time-squeezing discussed in Section 2 is more or less uniform throughout the entire undulator trajectory. Thus different parts of the trajectory contribute equally to the radiation amplitude. As  $K$  becomes larger so that the deflection angle  $\delta = K/\gamma$  is much larger than  $\gamma^{-1}$ , the time-squeezing becomes nonuniform and concentrated in small portions of the trajectory where the trajectory slope is within an angle  $\gamma^{-1}$  to the observation direction. Those portions of the trajectory can be replaced by segments of a circle. Therefore, the radiation from a large  $K$  undulator will be similar to that from a sequence of bending magnets. An undulator in such a case is usually referred to as a wiggler. In this section, we study the nature of the wiggler limit.



To see the nonuniformity of the time-squeezing quantitatively, we return to the apparent trajectory of the undulator discussed in Subsection 4.1. From Eq. (4.14), we obtain the scale-change factor in the forward direction,

$$\kappa = \frac{dt}{dt'} = \frac{\omega_u}{\omega_1(0)} \left( 1 + \frac{K^2}{1 + K^2/2} \cos(2\omega_u t') \right). \quad (5.1)$$

Thus, the scale-change factor is on the average  $\omega_u/\omega_1(0)$ , and, for  $K \lesssim 1$ , the scale change is more or less uniform. For  $K \gg 1$ , however, the scale change becomes much more pronounced around  $\omega_u t' = 2\pi(n \pm 1/2)$ , i.e., around those points where the trajectory slope is in the forward direction. At these points,  $\kappa$  is smaller by a factor  $(1 + K^2/2)^{-1}$  compared to its average value  $\omega_u/\omega_1(0)$ . Thus apparent trajectory will develop sharp kinks around these points at large  $K$ , as shown in Fig. 4.3. The strong acceleration of the apparent motion around these kinks will dominate the radiation.

The radius of the curvature at these points is

$$\rho = \frac{\gamma \lambda_u}{2\pi K}. \quad (5.2)$$

The spectrum from the individual kink is centered about the critical frequency  $\omega_c$  given by Eq. (3.7). Considered as an undulator, the harmonic number corresponding to  $\omega_c$  is

$$n_c = \frac{\omega_c}{\omega_1(0)} = \frac{3}{4} K (1 + K^2/2) \sim \frac{3}{8} K^3. \quad (5.3)$$

The bending-magnet approximation is valid in the frequency range where the harmonic number  $n = \omega/\omega_1(0)$  is of the order  $n_c$ .

For lower harmonics, an undulator cannot be approximated by a sequence of bending magnets even for a very large  $K$ . To see this, we recall that the opening angle of bending-magnet radiation is given by Eq. (3.24) or equivalently Eq. (3.28) (the low-frequency limit). This angle should be much less than  $\delta = K/\gamma$  in order that only small portions of the electron trajectory discussed in the above contribute to the radiation. Thus

$$\left( \frac{\lambda}{\rho} \right)^{1/3} \ll \frac{K}{\gamma}. \quad (5.4)$$

Inserting Eq. (5.2), and using

$$\lambda = \frac{\lambda_1}{n} = \frac{\lambda_u (1 + K^2/2)}{2\gamma^2 n},$$

we find that the inequality (5.4) becomes

$$n \gg 1. \quad (5.5)$$

Thus, both  $K$  and  $n$  must be much larger than unity for the wiggler approximation to be valid.

We now calculate the radiation amplitude assuming that  $K \gg 1$  and  $n \gg 1$  but taking into account the fact that more than one trajectory portions contribute to the radiation in multiperiod wigglers. In fact, there are  $2N$  trajectory portions in

an  $N$ -period wiggler since there are two points per period that are tangent to the observation direction. Figure 5.1 shows one period of the trajectory, and the two tangent points P and Q. For simplicity, we are assuming that the horizontal observation angle  $\varphi$  vanishes. However, we will keep the vertical angle  $\psi$  arbitrary. The radiation amplitude from the point P is

$$\begin{pmatrix} A_\sigma \\ A_\pi \end{pmatrix}_{n+} = \text{coeff} \exp i \left[ \pi(2n - 1/2)\omega/\omega_1(0) \right] \begin{pmatrix} K_{2/3}(\eta) \\ \frac{iX}{\sqrt{1+X^2}} K_{1/3}(\eta) \end{pmatrix} \quad (5.6)$$

This is the same as that given by Eq. (3.11), except for the phase factors which account for the fact that the tangent points are separated in time. The factor coeff in (5.6) is the coefficient in Eq. (3.11). The amplitude for the point Q is

$$\begin{pmatrix} A_\sigma \\ A_\pi \end{pmatrix}_{n-} = \text{coeff} \exp i \left[ \pi(2n + 1/2)\omega/\omega_1(0) \right] \begin{pmatrix} K_{2/3}(\eta) \\ \frac{-iX}{\sqrt{1+X^2}} K_{1/3}(\eta) \end{pmatrix} \quad (5.7)$$

Notice that the sign of the  $\pi$ -polarized term here is opposite to Eq. (5.6) because the curvature is pointing in the opposite direction. These two amplitudes correspond to elliptical polarizations in which the electric field rotates in opposite directions. Adding these two amplitudes, one obtains

$$\begin{pmatrix} A_\sigma \\ A_\pi \end{pmatrix}_n = \text{coeff} \cdot 2 \cdot \exp i \left[ 2n\pi\omega/\omega_1(0) \right] \begin{pmatrix} \cos \left[ \frac{\pi\omega}{2\omega_1(0)} \right] K_{2/3}(\eta) \\ \sin \left[ \frac{\pi}{2} \frac{\omega}{\omega_1(0)} \right] \frac{X}{\sqrt{1+X^2}} K_{1/3}(\eta) \end{pmatrix} \quad (5.8)$$

Here, the amplitudes for the two polarization components are relatively real corresponding to a linearly polarized radiation. This was discussed in Subsection 4.3.

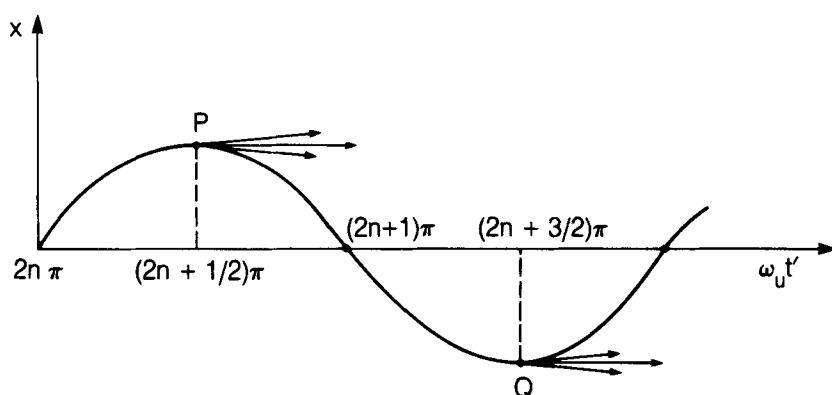


Figure 5.1 Illustration that wiggler radiation originates in small regions around the tangent points P and Q when observed in the  $z$ -direction.

Summing up contributions from different periods,  $n = 1, \dots, N$ , one finally obtains

$$\begin{pmatrix} A_\sigma \\ A_\pi \end{pmatrix} = \text{coeff} \cdot 2 \cdot \left( \frac{\sin N\pi\omega/\omega_1(0)}{\sin(\pi\omega/\omega_1(0))} \right) \begin{pmatrix} \cos \left( \frac{\pi\omega}{2\omega_1(0)} \right) \cdot K_{2/3}(\eta) \\ \sin \left( \frac{\pi\omega}{2\omega_1(0)} \right) \frac{X}{\sqrt{1+X^2}} K_{1/3}(\eta) \end{pmatrix} \quad (5.9)$$

The angular density of flux is obtained by inserting this expression into Eq. (2.41). The result is similar to Eq. (3.12), except that there is an overall factor

$$4 \cdot \left( \frac{\sin \left[ N\pi\omega/\omega_1(0) \right]}{\sin \pi \left[ \omega/\omega_1(0) \right]} \right)^2 \quad (5.10)$$

and additional factors  $\cos^2(\pi\omega/2\omega_1(0))$  and  $\sin^2(\pi\omega/2\omega_1(0))^2$  in the  $\sigma$ - and  $\pi$ -polarization components, respectively. The factor (5.10), which replaces the term  $N^2 S_N$  appearing in Eq. (4.24), represents the fact that the spectrum consists of the undulator harmonics.

We have found that, although the radiation from each tangent point for a large  $K$  can be approximated by the bending-magnet radiation, which has a smooth spectrum, the wiggler radiation, when all contributions from different tangent points are combined, exhibits sharp peaks at harmonics of  $\omega_1(0)$ . However, these peaks are extremely closely spaced at frequencies of interest  $\omega \sim \omega_c$ , the relative spacing being

$$\frac{\Delta\omega}{\omega} \Big|_{\text{sp}} \sim \frac{\omega_1}{\omega_c} = \frac{1}{n_c} \sim \frac{1}{K^3} \quad (5.11)$$

If the spectrum is averaged over frequency intervals larger than that given by Eq. (5.11), the spectrum will appear smooth. Indicating the average by angular brackets, we have

$$\left\langle \left( \frac{\sin N\pi\omega/\omega_1(0)}{\sin \pi\omega/\omega_1(0)} \right)^2 \right\rangle = N, \quad \left\langle \cos^2 \left( \frac{\pi\omega}{2\omega_1(0)} \right) \right\rangle = \frac{1}{2},$$

$$\left\langle \sin^2 \left( \frac{\pi\omega}{2\omega_1(0)} \right) \right\rangle = \frac{1}{2}.$$

Thus the averaged spectrum becomes

$$\begin{pmatrix} \frac{d^2 \mathcal{F}_\sigma}{d^2 \Omega} \\ \frac{d^2 \mathcal{F}_\pi}{d^2 \Omega} \end{pmatrix}_W = 2N \begin{pmatrix} \frac{d^2 \mathcal{F}_\sigma}{d^2 \Omega} \\ \frac{d^2 \mathcal{F}_\pi}{d^2 \Omega} \end{pmatrix}_B \quad (5.12)$$

where the subscript W and B represent the wiggler and bending magnet, respectively, the bending magnet spectrum being given by Eq. (3.12). Equation (5.12)

states that the wiggler radiation averaged in the sense described above appears to be an incoherent superposition of the radiation from  $2N$  wiggler poles.

The spectrum average can be achieved in several ways: One can use a monochromator whose relative bandwidth is larger than  $K^{-3}$ . Alternatively, if the radiation within a certain angular width  $\Delta\theta$  is collected, the angular broadening given by Eq. (4.34) will produce the required spectrum averaging if

$$\frac{\gamma^2 \Delta\theta^2}{1 + K^2/2} \gtrsim \frac{1}{K^3}, \text{ or } \Delta\theta \gtrsim \frac{1}{\gamma\sqrt{K}}. \quad (5.13)$$

The angular averaging is also achieved if the angular spread of the electron beam is larger than  $\Delta\theta$  given above.

So far, we have discussed the case where the horizontal observation angle  $\phi$  vanishes. For a nonvanishing  $\phi$ , the only modification is to use the proper expression for the radius of curvature  $\rho_\phi$  evaluated at the points tangent to the direction  $\phi$ . For a sinusoidal trajectory, this is given by

$$\rho_\phi = \rho \sqrt{1 - (\phi/\delta)^2}. \quad (5.14)$$

## 6 BRIGHTNESS, COHERENCE AND SYNCHROTRON RADIATION OPTICS

Our discussion of the radiation pattern so far has been limited to the angular distributions, i.e., the behavior at a large distance from the sources (the Fraunhofer zone). However, it is often the case that information on the radiation patterns at a finite distance from the sources (the Fresnel zone) is required. In particular, the synchrotron radiation is often focused by a suitable optical system to experimental samples. In that case, it is clearly desirable to know the flux distribution illuminating the image. These are illustrated in Fig. 6.1. Determining how radiation propagates through a general optical medium is the realm of optics. For synchrotron radiation optics, we need a more general framework than the flux distribution in the far field limit.

In principle, problems in synchrotron radiation optics can be solved completely by calculating the exact electric field based on Eq. (2.11) which takes into account the finite-distance effects [Hirai, et al., 1984]. In addition to being exceedingly complicated, such an approach is not satisfactory in the sense that the properties of the source cannot be clearly separated from those of the optical medium. Thus, the entire calculation beginning from the source needs to be repeated for problems involving the same source but different optical arrangements.

Here, we describe an approach to synchrotron radiation optics [Kim, 1986b; Coisson and Walker, 1986] that is modeled after the phase-space formulation of geometric optics. In this approach, the flux density in phase-space elements defined by the position and angle, called the brightness, plays a fundamental role: A source is completely characterized by its brightness distribution, and an optical medium by the transformation it causes on the brightness distribution. The brightness at each phase-space point is invariant under the optical transformation, and is therefore a true characterization of the radiation strength. Finally, the effects of the electron beam distribution are also transparent: The source brightness is given by a

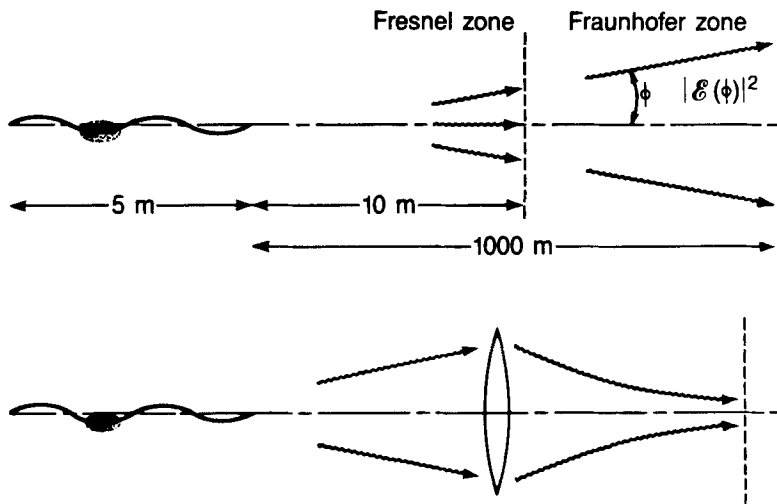


Figure 6.1 Finite distance effect in undulator radiation. The radiation is often observed at a distance comparable to the length of the undulator (top). The image of undulator radiation represents the radiation profile at the source itself (bottom).

convolution of the brightness due to an ideal electron and the electron beam distribution function.

### 6.1 Phase-Space Method in Geometric Optics

In optics, we study how the radiation generated by a source propagates through an optical medium as illustrated in Fig. 6.2.a. In geometric optics, diffraction effects are neglected and photons are considered as classical point particles. The phase-space method is a convenient way to describe geometric optics, and has been used extensively in accelerator physics for studying the transport of particle beams.

We introduce a few definitions: A trajectory of photon is called a ray. The ray of a reference photon is called the optical axis. A point along the optical axis is labeled by the  $z$ -coordinate. A plane normal to the optical axis is called the transverse plane. At a given transverse plane, we introduce the phase space spanned by the pair  $(\mathbf{x}, \boldsymbol{\varphi})$ , where  $\mathbf{x}$  and  $\boldsymbol{\varphi}$  are respectively the position and the direction with respect to the optical axis of the ray. In components, we have

$$\mathbf{x} = (x, y), \boldsymbol{\varphi} = (\varphi, \psi) \quad (6.1)$$

The distribution of the photon flux  $\mathcal{F}$  in phase space at  $z$  is specified by the brightness function defined by

$$\mathcal{B}(\mathbf{x}, \boldsymbol{\varphi}; z) = \frac{d^4 \mathcal{F}}{d^2 \mathbf{x} d^2 \boldsymbol{\varphi}} \quad (6.2)$$

The usefulness of the brightness function lies in the fact that those functions at two different transverse planes are related by a coordinate transformation which

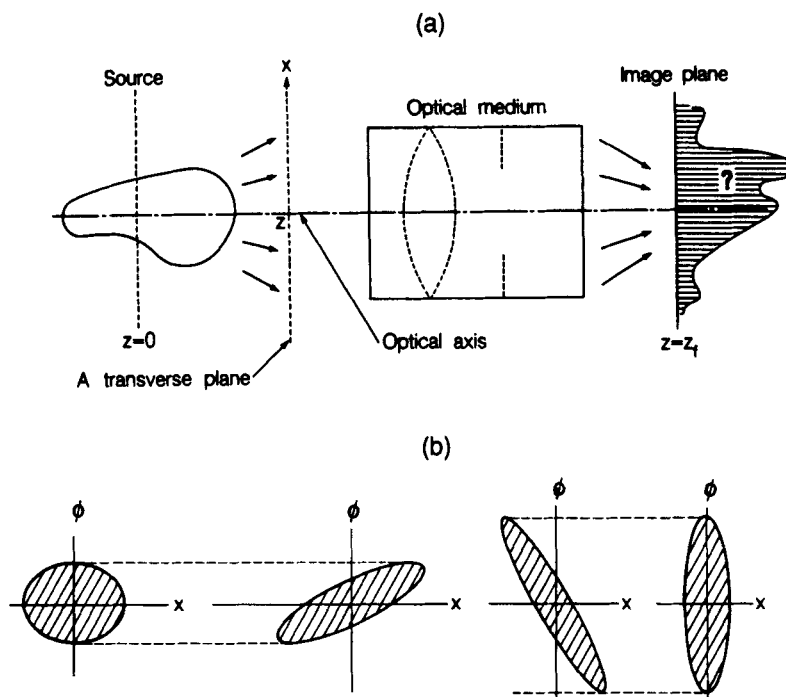


Figure 6.2 Propagation of radiation from source to the image plane. The problem of optics is to find the image profile (a). The phase-space distribution at any transverse plane along the optical axis can be represented by the phase-space diagram familiar in accelerator physics (b).

depends on the properties of the medium only. The transformation is especially simple when the rays remain close to the optical axis. In that case

$$\mathcal{B}(\mathbf{x}, \boldsymbol{\phi}; z_2) = \mathcal{B}(\mathbf{x}', \boldsymbol{\phi}'; z_1), \quad \begin{pmatrix} \mathbf{x}' \\ \boldsymbol{\phi}' \end{pmatrix} = M^{-1} \begin{pmatrix} \mathbf{x} \\ \boldsymbol{\phi} \end{pmatrix}. \quad (6.3)$$

Here  $M$  is a  $2 \times 2$  matrix given by a product of matrices — one for each lens and free space in between. These matrices are given by

$$M_\ell = \begin{pmatrix} 1 & \ell \\ 0 & 1 \end{pmatrix} \quad \text{for a free space of length } \ell, \quad (6.4a)$$

$$M_f = \begin{pmatrix} 1 & 0 \\ -1/f & 1 \end{pmatrix} \quad \text{for a lens of focal length } f. \quad (6.4b)$$

These transformations are well-known in particle beam optics. Figure 6.2.b illustrates the brightness transformation corresponding to Fig. 6.2.a in terms of the phase-space diagrams.

According to Eq. (6.3), the brightness at a given phase point on a transverse plane is the same as the brightness at the corresponding phase point on another

transverse plane. In particular, the brightness at the phase-space origin is invariant:

$$\mathcal{B}(0,0;z_1) = \mathcal{B}(0,0;z_2) = \mathcal{B}_0 . \quad (6.5)$$

The brightness at the phase-space origin  $\mathcal{B}_0$  will be sometimes referred for simplicity as the brightness. It is a measure of the intrinsic strength of a radiation source.

The transformation through an aperture is given by

$$\mathcal{B}_f(\mathbf{x},\boldsymbol{\varphi}) = S_\Delta(\mathbf{x}) \mathcal{B}_i(\mathbf{x},\boldsymbol{\varphi}) , \quad (6.6)$$

where  $S_\Delta$  is a function representing the fractional transmission across the aperture.

Integrating the brightness over the angles or positions, we obtain the angular or the spatial density of flux:

$$\frac{d^2\mathcal{F}}{d^2\boldsymbol{\varphi}} = \int \mathcal{B}(\mathbf{x},\boldsymbol{\varphi};z) d^2\mathbf{x} , \quad (6.7)$$

$$\frac{d^2\mathcal{F}}{d^2\mathbf{x}} = \int \mathcal{B}(\mathbf{x},\boldsymbol{\varphi};z) d^2\boldsymbol{\varphi} . \quad (6.8)$$

The angular density of flux, Eq. (6.7), which we have discussed extensively for the case of synchrotron radiation, is sometimes called brightness. However, it is not an invariant measure of the source strength, and we will reserve the term brightness for  $\mathcal{B}$ . Finally, one obtains the flux by integration, as follows:

$$\mathcal{F} = \int \frac{d^2\mathcal{F}}{d^2\mathbf{x}} d^2\mathbf{x} = \int \frac{d^2\mathcal{F}}{d^2\boldsymbol{\varphi}} d^2\boldsymbol{\varphi} = \int \mathcal{B}(\mathbf{x},\boldsymbol{\varphi};z) d^2\mathbf{x} d^2\boldsymbol{\varphi} . \quad (6.9)$$

The flux is another invariant.

The various differential fluxes in the above are understood to be *spectral* quantities, i.e., the fluxes in an infinitesimally small bandwidth around a given frequency. To be precise, therefore, we should call  $\mathcal{B}$  the spectral brightness,  $d^2\mathcal{F}/d^2\boldsymbol{\varphi}$ , the angular density of spectral flux, and so on. However, we often drop the adjective spectral for the sake of brevity.

## 6.2 Phase-Space Method in Wave Optics

A wave cannot be represented by classical particles. Therefore, the concepts of phase space and brightness lose the obvious physical meaning in wave optics. Nevertheless, it turns out to be possible to construct a quantity that is bilinear in the electric field and that behaves almost the same as the brightness in geometric optics. The phase-space method in wave optics is based on this quantity, which we call the brightness in wave optics.

We start from the electric field in the frequency domain, Eq. (2.19). Since we will be always working with a fixed frequency,  $\omega$ , the frequency dependence will be suppressed to simplify the notations. The three-dimensional vector  $\mathbf{x}$  in Eq. (2.19) has the transverse component  $\mathbf{x}$  (which is a two-dimensional vector in our current notation) and the longitudinal component  $z$  which is the location of the transverse plane. Thus we write

$$E(\mathbf{x},\omega) = E(\mathbf{x};z) . \quad (6.10)$$

In the above, the LHS is the notation of Eq. (2.19), while the RHS is in the current notations.

In this section, we will regard the electric field to be a scalar. For synchrotron radiation considered in previous sections, we can take the scalar electric field to be the  $\sigma$ -polarized component, which is usually the dominant one.

We work with the pair consisting of the coordinate representation  $E(\mathbf{x};z)$  and its angular representation  $\mathcal{E}(\boldsymbol{\varphi};z)$ :

$$\mathcal{E}(\boldsymbol{\varphi};z) = \frac{1}{\lambda^2} \int E(\mathbf{x};z) e^{-i\mathbf{k}\boldsymbol{\varphi} \cdot \mathbf{x}} d^2\mathbf{x} \quad , \quad (6.11a)$$

$$E(\mathbf{x};z) = \int \mathcal{E}(\boldsymbol{\varphi};z) e^{i\mathbf{k}\boldsymbol{\varphi} \cdot \mathbf{x}} d^2\boldsymbol{\varphi} \quad . \quad (6.11b)$$

To understand the meaning of the angular representation, assume that the space between  $z$  and  $z + \ell$  is free. From Maxwell's equation, we must have

$$\mathcal{E}(\boldsymbol{\varphi};z + \ell) = \mathcal{E}(\boldsymbol{\varphi};z) e^{\pm i\mathbf{k}\sqrt{1-\boldsymbol{\varphi}^2}\ell} \quad .$$

Assuming that the radiation source is located at  $z_s < z$  the wave must propagate to the positive  $z$  direction. Thus we pick the plus sign in the exponent. Also, we assume that the wave is concentrated near the forward direction so that

$$\sqrt{1-\boldsymbol{\varphi}^2} \approx 1 - \frac{\boldsymbol{\varphi}^2}{2} \quad . \quad (6.12)$$

We then obtain

$$\mathcal{E}(\boldsymbol{\varphi};z + \ell) = \mathcal{E}(\boldsymbol{\varphi};z) e^{i\mathbf{k}(1-\boldsymbol{\varphi}^2/2)\ell} \quad . \quad (6.13)$$

Equation (6.13) is the Fresnel's diffraction in the angular representation. From Eqs. (6.11b), (6.13) and the relation

$$\lim_{\ell \rightarrow +\infty} e^{\pm i\ell x^2} = e^{\pm \frac{\pi}{4}i} \sqrt{\frac{\pi}{\ell}} \delta(x) \quad ,$$

we can derive the following result:

$$\lambda \mathcal{E}(\boldsymbol{\varphi};z) = \lim_{\ell \rightarrow \infty} i\ell E(\ell\boldsymbol{\varphi};z + (1 - \boldsymbol{\varphi}^2/2)\ell) e^{-i\mathbf{k}\ell} \quad . \quad (6.14)$$

Equation (6.14) is an optical reciprocity statement that the far-field pattern is equivalent to the Fourier transform of the near-field pattern.

The brightness in wave optics is defined as follows:

$$\begin{aligned} \mathcal{B}(\mathbf{x}, \boldsymbol{\varphi};z) &= \frac{d\omega}{\hbar\omega} \frac{2\varepsilon_0 c}{T} \int d^2\xi \langle \mathcal{E}^*(\boldsymbol{\varphi} + \boldsymbol{\xi}/2; z) \mathcal{E}(\boldsymbol{\varphi} - \boldsymbol{\xi}/2; z) \rangle e^{-i\mathbf{k}\boldsymbol{\xi} \cdot \mathbf{x}} \quad , \\ &= \frac{d\omega}{\hbar\omega} \frac{2\varepsilon_0 c}{T\lambda^2} \int d^2\mathbf{y} \langle E^*(\mathbf{x} + \mathbf{y}/2; z) E(\mathbf{x} - \mathbf{y}/2; z) \rangle e^{i\mathbf{k}\boldsymbol{\varphi} \cdot \mathbf{y}} \quad . \end{aligned} \quad (6.15)$$

Here  $T$  is the time duration of the electric field so that  $\mathcal{B}T$  can be interpreted as the total number of photons per unit phase-space area into the spectral bandwidth  $d\omega$ . The angular brackets in the above represent averaging over an appropriate statistical ensemble in case the field contains fluctuating parts. It can be shown from Eq. (6.11) that the two representations of the brightness in the above are



equivalent. Equation (6.15) is a Wigner distribution function of the electric fields [Wigner, 1932].

The phase-space variable  $(\mathbf{x}, \boldsymbol{\phi})$  and the brightness as introduced in the above are mathematical constructions not directly related to physically measurable quantities. However, we can show that the brightness defined by Eq. (6.15) behaves almost as if it is the real flux density in real phase space: First, by integrating over  $\mathbf{x}$  or  $\boldsymbol{\phi}$ , we can establish Eqs. (6.7) and (6.8). Notice that the quantities in the LHS of these equations are physically measurable, positive definite quantities. Second, one can demonstrate the validity of the transformation property, Eq. (6.3): For free space, it follows from Eqs. (6.13) and (6.15) that

$$\mathcal{B}(\mathbf{x}, \boldsymbol{\phi}; z + \ell) = \mathcal{B}(\mathbf{x} - \ell \boldsymbol{\phi}, \boldsymbol{\phi}; z) . \quad (6.16)$$

This is equivalent to Eq. (6.3) and (6.4a). The proof for the lens transformation is similar and is based on the relation (see for example, Goodman, 1968)

$$E_{\text{after}}(\mathbf{x}; z) = E_{\text{before}}(\mathbf{x}; z) e^{ikx^2/2f} . \quad (6.17)$$

When diffraction effects become important, the brightness in wave optics behaves differently from the brightness in geometric optics. Thus, the transformation through an aperture in the present case is given by

$$\mathcal{B}_f(\mathbf{x}, \boldsymbol{\phi}) = \int G(\mathbf{x}, \boldsymbol{\phi} - \boldsymbol{\phi}') \mathcal{B}_i(\mathbf{x}, \boldsymbol{\phi}') d^2 \boldsymbol{\phi}' . \quad (6.18)$$

Here

$$G(\mathbf{x}, \boldsymbol{\phi}) = \frac{1}{\lambda^2} \int d^2 \mathbf{y} S_{\Delta}^*(\mathbf{x} + \mathbf{y}/2) S_{\Delta}(\mathbf{x} - \mathbf{y}/2) e^{ik\boldsymbol{\phi} \cdot \mathbf{y}} . \quad (6.19)$$

The brightness in wave optics defined by Eq. (6.15) is not positive definite and thus cannot be identified as a genuine phase-space density of flux. This is unavoidable because of the diffraction. The phase-space method is nevertheless useful for wave-optics calculations which proceed as follows: The source is specified by the brightness at the source plane  $z = 0$ . The propagation through an optical medium is represented by a series of brightness transformations given above. The physically measurable quantities at the image plane are obtained by integrations, Eq. (6.7) or (6.8).

### 6.3 Gaussian Laser Beam

The simplest solution of the paraxial wave equation in free space is (see for example, Yariv, 1975)

$$E(\mathbf{x}, z) = E_0 \frac{w_0}{w(z)} \times \exp \left\{ i \left[ kz - \tan^{-1} \left( \frac{z}{z_R} \right) \right] - \mathbf{x}^2 \left[ \frac{1}{w^2(z)} - \frac{ik}{2R(z)} \right] \right\} , \quad (6.20)$$

where

$$\begin{aligned}
 w^2(z) &= w_0^2(1 + z^2/z_R^2) , \\
 z_R &= \pi w_0^2/\lambda = kw_0^2/2 , \\
 R(z) &= z(1 + z_R^2/z^2) .
 \end{aligned} \tag{6.21}$$

The quantities  $w_0$  and  $z_R$  are usually known as the waist and the Rayleigh range, respectively. This solution described the Gaussian laser beam. Inserting Eq. (6.20) into Eq. (6.15), we obtain the corresponding brightness distribution function

$$\mathcal{B}(\mathbf{x}, \boldsymbol{\varphi}; z) = \mathcal{B}_0 \exp \left\{ -\frac{1}{2} \left[ \frac{(\mathbf{x} - z\boldsymbol{\varphi})^2}{\sigma_r^2} + \frac{\boldsymbol{\varphi}^2}{\sigma_r'^2} \right] \right\} . \tag{6.22}$$

Here

$$\sigma_r = w_0/2 , \tag{6.23a}$$

$$\sigma_r' = \sigma_r/z_R = 1/kw_0 . \tag{6.23b}$$

We see that Eq (6.22) satisfies the free-space transformation rule, Eq. (6.16).

The quantities  $\sigma_r$  and  $\sigma_r'$  are the rms transverse size and angular divergence, respectively, of the laser beam at  $z = 0$ . From Eq. (6.23), it follows that

$$\sigma_r \sigma_r' = \lambda/4\pi . \tag{6.24}$$

$$\sigma_r/\sigma_r' = z_R . \tag{6.25}$$

The quantity corresponding to (6.24) for electron beams is the emittance, and that corresponding to  $z_R$  is the so-called beta function.

By integrating Eq (6.22), and comparing the result with Eq. (6.9), we obtain the expression for the brightness at the phase-space origin

$$\mathcal{B}_0 = \frac{\mathcal{F}}{(2\pi\sigma_r\sigma_r')^2} = \frac{\mathcal{F}}{(\lambda/2)^2} . \tag{6.26}$$

The quantity  $2\pi\sigma_r\sigma_r'$  can thus be interpreted as the phase-space area in one transverse dimension. The phase-space area for the Gaussian laser beam is therefore  $\lambda/2$  in each transverse dimension.

#### 6.4 Effect of Electron Distribution on Brightness of Synchrotron Radiation [Kim, 1986b]

For synchrotron radiation, the single-electron brightness can be calculated from the explicit expression of the electric field in the coordinate representation, Eq. (2.11). It is, however, simpler to use the angular representation because it is equivalent to the far-field pattern in view of Eq. (6.14). By comparing with the results of Subsection 2.4.2, we obtain

$$\mathcal{E}(\boldsymbol{\varphi}; 0) = \frac{e}{4\pi\epsilon_0 c} \frac{\omega}{\lambda\sqrt{2\pi}} \int dt' \mathbf{n} \times \left[ \mathbf{n} \times \boldsymbol{\beta}(t') \right] e^{i\omega t(t')} . \tag{6.27}$$

Here  $\mathbf{n} = (\boldsymbol{\varphi}, 1 - \boldsymbol{\varphi}^2/2)$ . The brightness of synchrotron radiation can be calculated explicitly by inserting Eq. (6.27) into Eq. (6.15). Before discussing this, we wish to

establish an important result concerning the effect of the electron beam size and angular divergence.

For this purpose, consider the electron trajectories passing the plane at  $z = 0$ . The reference electron passes the plane at  $t = 0$  and the  $i$ th electron at  $t = t^i$  at the position  $\mathbf{x}_e^i$  and the angle  $\boldsymbol{\varphi}_e^i$  relative to the reference electron trajectory. Assuming that the focusing force on electrons is negligible, it can be derived that

$$\mathcal{E}_i(\boldsymbol{\varphi}; 0) = \exp i\omega(t - \boldsymbol{\varphi} \cdot \mathbf{x}_e^i/c) \mathcal{E}^0(\boldsymbol{\varphi} - \boldsymbol{\varphi}_e^i, 0) . \quad (6.28)$$

Here  $\mathcal{E}^0$  and  $\mathcal{E}_i$  are respectively the electric field due to the reference electron and the  $i$ th electron, respectively. Since the total electric field is given by

$$\mathcal{E}(\boldsymbol{\varphi}; 0) = \sum_i \mathcal{E}_i(\boldsymbol{\varphi}; 0) ,$$

we calculate the following ensemble average:

$$\begin{aligned} \langle \mathcal{E}^*(\boldsymbol{\varphi}_1; 0) \mathcal{E}(\boldsymbol{\varphi}_2; 0) \rangle &= \sum_{i=1}^{N_e} \langle \mathcal{E}_i^*(\boldsymbol{\varphi}_1; 0) \mathcal{E}_i(\boldsymbol{\varphi}_2; 0) \rangle \\ &+ \sum_{i \neq j} \langle \mathcal{E}_i^*(\boldsymbol{\varphi}_1; 0) \mathcal{E}_j(\boldsymbol{\varphi}_2; 0) \rangle , \end{aligned} \quad (6.29)$$

where  $N_e$  is the total number of electrons. In view of Eq. (6.28) the second term in the above contains the factor

$$\langle \exp i\omega(t_i - t_j) \rangle_{i \neq j} = \left| \int e^{ikz} f_z(z) dz \right|^2 .$$

Here  $f_z(z)dz$  is the probability to find an electron between the longitudinal position  $z$  and  $z+dz$ . Assuming the Gaussian distribution,

$$f_z(z) = \frac{1}{\sqrt{2\pi} \sigma_z} \exp \left[ -z^2/2\sigma_z^2 \right] ,$$

where  $\sigma_z$  is the rms bunch length, we obtain

$$\langle \exp i\omega(t_i - t_j) \rangle_{i \neq j} = \exp \left[ -k^2 \sigma_z^2 \right] . \quad (6.30)$$

It is usually the case that

$$N_e \exp \left[ -k^2 \sigma_z^2 \right] \ll 1 .$$

In this case, we can neglect the off-diagonal terms ( $i \neq j$ ) in Eq. (6.29), and obtain

$$\langle \mathcal{E}^*(\boldsymbol{\varphi}_1; 0) \mathcal{E}(\boldsymbol{\varphi}_2; 0) \rangle = N_e \langle \exp i \left[ k \mathbf{x}_e^i \cdot (\boldsymbol{\varphi}_1 - \boldsymbol{\varphi}_2) \right] \mathcal{E}^{0*}(\boldsymbol{\varphi}_1 - \boldsymbol{\varphi}_e^i) \mathcal{E}^0(\boldsymbol{\varphi}_2 - \boldsymbol{\varphi}_e^i) \rangle .$$

Inserting this into the definition of the brightness, we obtain

$$\begin{aligned} \mathcal{B}(\mathbf{x}, \boldsymbol{\varphi}; 0) &= N_e \langle \mathcal{B}^0 \left[ \mathbf{x} - \mathbf{x}_e^i, \boldsymbol{\varphi} - \boldsymbol{\varphi}_e^i; 0 \right] \rangle \\ &= N_e \int \mathcal{B}^0(\mathbf{x} - \mathbf{x}_e, \boldsymbol{\varphi} - \boldsymbol{\varphi}_e; 0) f(\mathbf{x}_e, \boldsymbol{\varphi}_e; 0) d^2 \mathbf{x}_e d^2 \boldsymbol{\varphi}_e . \end{aligned} \quad (6.31)$$

In the above  $\mathcal{B}$  is the total brightness,  $\mathcal{B}^0$  is the brightness due to the reference electron. The function  $f$  is the probability distribution function in the electron

phase space  $(\mathbf{x}_e, \boldsymbol{\varphi}_e)$ . If  $z = 0$  is the symmetry point in a straight section, it is of the following form:

$$f(\mathbf{x}_e, \boldsymbol{\varphi}_e; 0) = \frac{1}{(2\pi)^2 \varepsilon_x \varepsilon_y} \exp \left[ -\frac{1}{2} \left\{ \frac{x_e^2}{\sigma_x^2} + \frac{\varphi_e^2}{\sigma_{x'}^2} + \frac{y_e^2}{\sigma_y^2} + \frac{\psi_e^2}{\sigma_{y'}^2} \right\} \right], \quad (6.32)$$

where  $\varepsilon_x = \sigma_x \sigma_{x'}$  and  $\varepsilon_y = \sigma_y \sigma_{y'}$  are known as the electron beam emittances in the  $x$  and  $y$  directions, respectively.

Neglecting the space-charge forces, the electron movement in storage rings obeys geometric optics. See, for example, Sands (1970). The electrons' phase-space distribution function correspond to the brightness function for radiation. Equation (6.31) is similar in appearance to the convolution of two probability functions, and will be referred to as the brightness convolution theorem.

Integrating (6.31) over  $\mathbf{x}$ , we find that the convolution theorem holds for angular densities also:

$$\frac{d^2 \mathcal{F}}{d^2 \boldsymbol{\varphi}}(\boldsymbol{\varphi}) = \int \frac{d^2 \mathcal{F}^0}{d^2 \boldsymbol{\varphi}}(\boldsymbol{\varphi} - \boldsymbol{\varphi}_e) g(\boldsymbol{\varphi}_e) d^2 \boldsymbol{\varphi}_e, \quad (6.33)$$

where

$$g(\boldsymbol{\varphi}_e) = \int f(\mathbf{x}_e, \boldsymbol{\varphi}_e; 0) d^2 \mathbf{x}_e.$$

Application of Eq. (6.33) was discussed in Subsection 4.2.4.

## 6.5 Brightness of Undulator Radiation

The electric field in the angular representation for the case of undulators is proportional to Eq. (4.22). Although the exact calculation of the brightness function is complicated, we can obtain an approximate expression by neglecting the variation in angles of the last factor in Eq. (4.22). One obtains at  $\omega = n\omega_1(0)$

$$\mathcal{B}^0(\mathbf{x}, \boldsymbol{\varphi}) = \frac{\mathcal{F}^0}{(\lambda/2)^2} \left\{ \frac{2}{\pi L} \int_{-L/2}^{L/2} d\mathbf{x} \int_0^{\frac{L}{2} - \mathbf{x}} \frac{d\ell}{\ell} \sin k \left( \frac{(\mathbf{x} - \mathbf{x}\boldsymbol{\varphi})^2}{\ell} - \ell \boldsymbol{\varphi}^2 \right) \right\}. \quad (6.34)$$

The function in the curly brackets in the above is normalized to unity at  $\mathbf{x} = \boldsymbol{\varphi} = 0$ . Thus

$$\mathcal{B}^0(0,0;0) = \frac{\mathcal{F}^0}{(\lambda/2)^2}. \quad (6.35)$$

Here  $\mathcal{F}^0$  is the flux contained in the central cone for a single electron. The shape of the brightness function is plotted in Fig. 6.3 for the case the vectors  $\mathbf{x}$  and  $\boldsymbol{\varphi}$  are parallel to each other.

For simple calculation, we will approximate the shape of the undulator brightness by that of the Gaussian laser beam given by Eq. (6.22). Note that Eq. (6.35) is consistent with Eq. (6.26). The rms angular width  $\sigma_r$  of the undulator radiation was determined before by Eq. (4.33). The source size  $\sigma_r$  is determined by Eq.

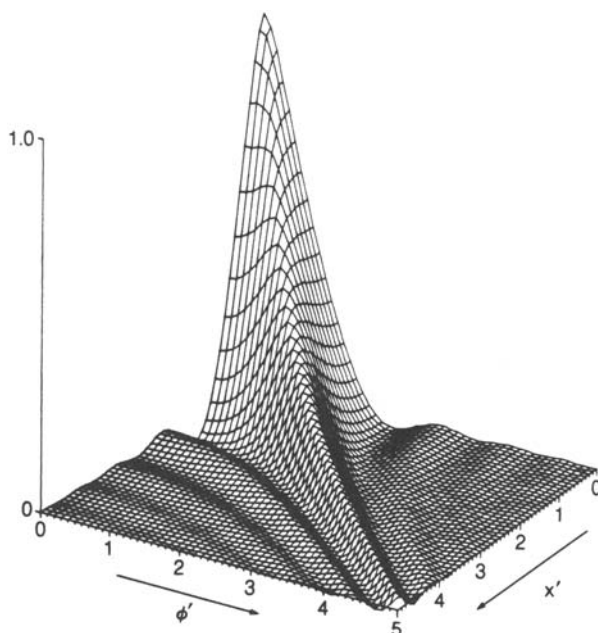


Figure 6.3 The undulator brightness function at  $\omega = \omega_1(0)$  for the case  $\mathbf{x}$  and  $\boldsymbol{\varphi}$  are parallel.

(6.24). Thus the undulator brightness function for a single electron is approximated by

$$\mathcal{B}^0(\mathbf{x}, \boldsymbol{\varphi}; 0) = \frac{\mathcal{B}^0(0,0;0)}{(\lambda/2)^2} \exp - \frac{1}{2} \left[ \frac{\mathbf{x}^2}{\sigma_r^2} + \frac{\boldsymbol{\varphi}^2}{\sigma_r^2} \right], \quad (6.36)$$

where

$$\sigma_r = \sqrt{2\lambda L} / 4\pi, \quad \sigma_r = \sqrt{\lambda/2L}. \quad (6.37)$$

Taking into account the electron beam effects, we carry out the convolution integral Eq. (6.31). We obtain

$$\mathcal{B}_0 = \mathcal{B}(0,0;0) = \frac{\mathcal{F}}{(2\pi)^2 \sigma_{Tx} \sigma_{Tx'} \sigma_{Ty} \sigma_{Ty'}}, \quad (6.38)$$

where  $\sigma_{Tx'}$  and  $\sigma_{Ty'}$  are given in Eq. (4.50), and

$$\begin{aligned} \sigma_{Tx} &= \sqrt{\sigma_r^2 + \sigma_x^2} \\ \sigma_{Ty} &= \sqrt{\sigma_r^2 + \sigma_y^2}. \end{aligned} \quad (6.39)$$

In Eq. (6.38),  $\mathcal{F}$  is the flux into the central core given by Eq. (4.46). The following limiting cases are of interest:

$$(A) \quad \sigma_x, \sigma_y \gg \sigma_r \text{ and } \sigma_x', \sigma_y' \gg \sigma_r' ;$$

$$\mathcal{B}_0 = \frac{\mathcal{F}}{(2\pi)^2 \varepsilon_x \varepsilon_y} \quad (6.40)$$

$$(B) \quad \sigma_x, \sigma_y \gg \sigma_r \text{ and } \sigma_x', \sigma_y' \ll \sigma_r' ;$$

$$\mathcal{B}_0 = \frac{\mathcal{F}}{(2\pi)^2 \sigma_r^2 \sigma_x \sigma_y} \quad (6.41)$$

$$(C) \quad \sigma_x, \sigma_y \ll \sigma_r \text{ and } \sigma_x', \sigma_y' \ll \sigma_r' ;$$

$$\mathcal{B}_0 = \frac{\mathcal{F}}{(2\pi)^2 \sigma_r^2 \sigma_r'^2} = \frac{\mathcal{F}}{(\lambda/2)^2} \quad (6.42)$$

Equation (6.42) gives the ultimate brightness achievable from undulators. Since  $\mathcal{F}$  scales as  $N$ , the number of undulator periods, the peak brightness scales as  $N$  both in the electron emittance dominated regime (A) and the diffraction dominated regime (C). In the intermediate regime (B), the brightness scales as  $N^2$  since  $\sigma_r$  scales as  $N^{-1/2}$ . Since  $\sigma_r$  and  $\sigma_r'$  are both proportional to  $\sqrt{\lambda}$ , the different regimes in the above correspond to different wavelength regions.

In order to fully utilize the high brightness of the undulator radiation, the electron beam needs to be bright, i.e., its emittance small and its current high. There are several proposals for the next-generation synchrotron radiation facilities. These are all based on low-emittance ( $\varepsilon_x$  less than  $10^{-8}$  m-r), high current (several hundred mA) electron or positron storage rings, and optimized for the undulator operation in straight sections. Of these, the 6–7 GeV machines [Shenoy and Moncton, 1988; Haensel, 1988] are optimum for hard x-rays, the undulator operation being in the regime (A) described in the above. The 1–2 GeV machines [LBL, 1986] are on the other hand optimized for the vacuum-ultraviolet

and the soft x-ray radiation, the undulator operation being in a regime between (B) and (C). Figure 6.4 shows the spectral brightness for different synchrotron radiation sources.

## 6.6 Brightness of Bending Magnet and Wiggler Radiation

As we have discussed in Section 2 and also in Section 5, the radiation for wigglers and bending magnets is emitted mainly in the direction parallel to the instantaneous motion of the electron. Assuming that photons from different points of the trajectory are incoherent, the brightness due to a single electron can be approximated by

$$\mathcal{B}^0(x, y, \varphi, \psi; 0) = \frac{d^2 \mathcal{F}^0}{d^2 \Omega} \sum \delta \left( x - \bar{x}(\varphi) + \varphi \bar{z}(\varphi) \right) \delta \left( y + \psi \bar{z}(\varphi) \right) .$$

Here  $d^2 \mathcal{F}^0 / d^2 \Omega$  is the angular density discussed in Sections 3 and 5, and  $\bar{x}(\varphi)$  and  $\bar{z}(\varphi)$  are the  $x$  and  $z$  coordinates, respectively, of the point where the trajectory slope is  $\varphi$ . A ray emitted at that point appears to have originated from the position  $x = \bar{x}(\varphi) - \varphi \bar{z}(\varphi)$  and  $y = -\psi \bar{z}(\varphi)$  in the  $z = 0$  plane, as explained in Fig. 6.5.

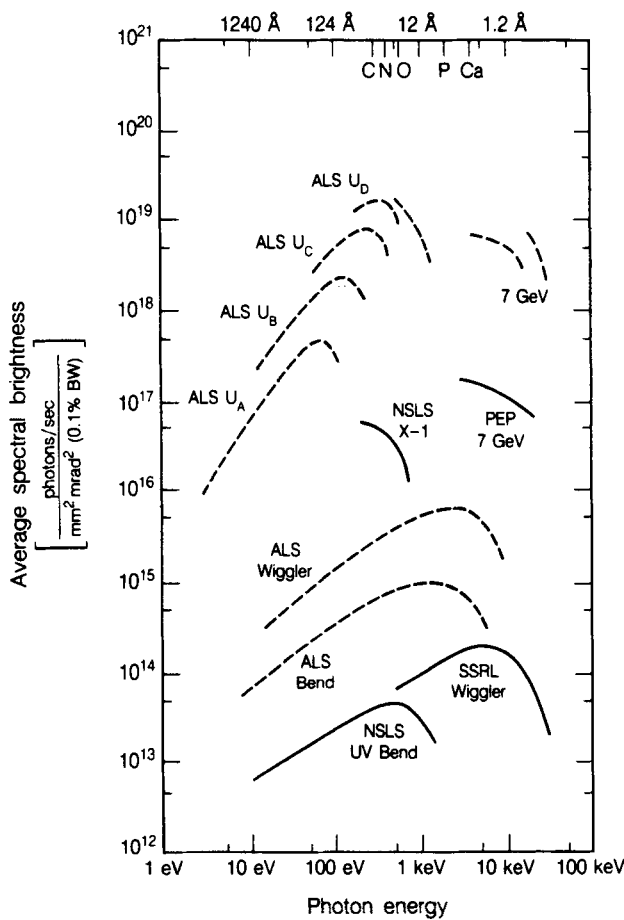


Figure 6.4 Average spectral brightness within a 0.1% bandwidth, as a function of photon energy, for a variety of synchrotron radiation sources.

There are, in general, a multiplicity of such points. The summation in the above is over those points.

The brightness from wigglers on bending magnets taking into account the electron beam effects is obtained by Eq. (6.30). We will not go in to the details of such calculations here since the emphasis of the bending-magnet or wiggler radiation is not the brightness but the flux.

6.7 Coherence

The coherence is a unique feature for a wave, and is a measure of how sharp the interference patterns can develop [Born and Wolf, 1980]. Two types of coherence can be distinguished: the transverse coherence refers to the coherence of the electromagnetic disturbances at two points on a transverse plane at a given time. The temporal coherence refers to the case of two points separated in time.

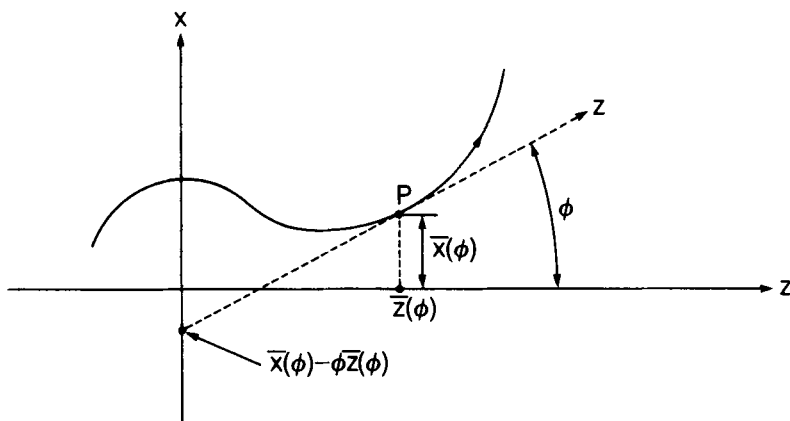


Figure 6.5 Determination of source coordinates at  $z = 0$  for radiation observed at an angle  $\phi$ . The source point is the intersection of a straight line, whose slope is  $\phi$  and which is tangent to the curve, and the source plane.

The temporal coherence is characterized by the coherence length,  $\ell_c$ , which is the length over which the wave maintains a definite phase relationship. It is related to the spectral bandwidth by

$$\ell_c = \lambda(\lambda/\Delta\lambda) = \lambda^2/\Delta\lambda \quad (6.43)$$

Thus undulator radiation observed through a small pinhole will have the coherence length  $\ell_c \sim N\lambda_1$  as discussed in Subsection 4.2.1.

The degree of the transverse coherence is determined by the phase-space area occupied by the radiation. To see this, consider a simple thought experiment as shown in Fig. 6.6: The radiation from a source passes through a pair of pinholes at  $z$  and forms an interference pattern at an image plane far away from the pinholes. The pinhole pair is symmetrically placed with respect to the optical axis to test the transverse coherence. Let  $\mathbf{x}$  and  $-\mathbf{x}$  be the position of the pinholes, and  $d^2\mathbf{x} = dx dy$  the area of the individual pinhole. The interference pattern consists of a smooth background and an oscillatory part having maxima and minima. The partial flux contained in the latter part can be shown to be

$$d^2\mathcal{F}_{\text{int}} = 2 \frac{d\omega}{\hbar\omega} \frac{2\varepsilon_0 c}{T} \left| \langle E^*(\mathbf{x}; z) E(-\mathbf{x}; z) \rangle \right| d^2\mathbf{x} \quad (6.44)$$

The partial flux contained in the smooth background is

$$d^2\mathcal{F}_{\text{b.g.}} = d^2\mathcal{F} - d^2\mathcal{F}_{\text{int}} \quad (6.45)$$

where  $d^2\mathcal{F}$  is the flux entering the pinholes. Adding these partial fluxes from different pinhole locations, we obtain



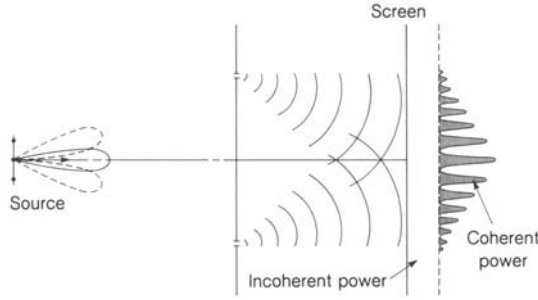


Figure 6.6 Schematic of an interference experiment to determine the transverse coherence.

$$\begin{aligned} \mathcal{F}_{\text{int}} &= \frac{d\omega}{\hbar\omega} \frac{2\epsilon_0 c}{T} \int d^2\mathbf{x} \left| \langle E^*(\mathbf{x};z) E(-\mathbf{x};z) \rangle \right| \\ &= \frac{1}{4} \int d^2\mathbf{x} \left| \int d^2\boldsymbol{\varphi} e^{-i\mathbf{k}\boldsymbol{\varphi} \cdot \mathbf{x}} \mathcal{B}(0,\boldsymbol{\varphi};z) \right| \\ &\geq (\lambda/2)^2 \mathcal{B}_0 \quad , \end{aligned} \tag{6.46}$$

$$\mathcal{F}_{\text{b.g.}} = \mathcal{F} - \mathcal{F}_{\text{int}} \geq 0 \quad . \tag{6.47}$$

From Eqs. (6.46) and (6.47), it follows that

$$\frac{\mathcal{F}}{\mathcal{B}_0} \geq (\lambda/2)^2 \quad . \tag{6.48}$$

The ratio  $\mathcal{F}/\mathcal{B}_0$  in the above may be identified as the phase-space area of the radiation beam. The inequality [Eq. (6.48)] is the statement that the minimum possible phase-space area in wave optics is  $(\lambda/2)^2$ . It also follows from the above argument that if the phase-space area associated with a radiation beam is determined to be the minimum possible value  $(\lambda/2)^2$ , then it will exhibit a sharp interference pattern without a smooth background for any pinhole pair symmetrically placed about the optical axis. We are therefore justified to introduce the transversely coherent flux  $\mathcal{F}_{\text{coh}}$  associated with a radiation beam by

$$\mathcal{F}_{\text{coh}} = (\lambda/2)^2 \mathcal{B}_0 \quad . \tag{6.49}$$

Note that this is an invariant quantity since the peak brightness is invariant.

From Eq. (6.26), we see that the Gaussian laser mode is completely transversely coherent.

It is instructive to illustrate the phase-space treatment of transverse coherence with an example. We shall give a simple explanation of the well-known fact that incoherent radiation can be made coherent by introducing aperture. To simplify the discussion, we consider one transverse dimension only. A source of width  $2a$  emitting uniformly in all angles ( $\Delta\varphi \sim 1$ ) occupies an area  $2a$  in phase space as shown in Fig. 6.7a. The source is incoherent if  $a \gg \lambda$ . At a distance  $z$  from the

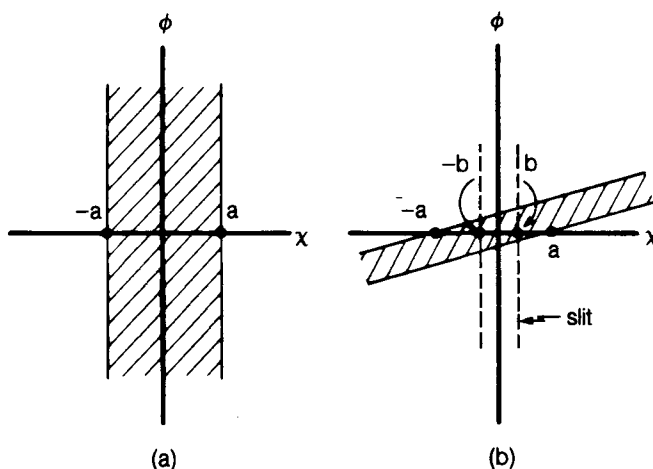


Figure 6.7 The phase space of an incoherent source (a) and the transformed diagram at a large distance from the source (b). The phase-space area between the lines  $x = -b$  and  $x = b$  can be made less than  $\lambda/2$  leading to transverse coherence.

source, the phase-space distribution is tilted in view of Eq. (6.16). This is shown in Fig. 6.7b. The angular width at any transverse position is  $2a/z$ . If one introduces a slit of width  $2b$ , as indicated by the broken lines in the figure, the phase-space area becomes  $4ab/z$ . According to the criteria developed in the above, the radiation will be transversely coherent if  $4ab/z \lesssim \lambda/2$ , in rough agreement with the well-known result in optics.

As the coherent flux is directly related to the brightness, the high brightness of undulator radiation means that the undulator radiation is also highly coherent [Kondratenko and Skrinsky (1977); Kim (1986b)]. In particular, the undulator radiation is completely coherent if the electron-beam phase space is small, i.e., in the regime (C) discussed in Subsection 6.5.

The power contained in the coherent flux given by Eq. (6.49) is

$$\hbar\omega \mathcal{F}_{\text{coh}} = \hbar\omega(\lambda/2)^2 \mathcal{B}_0 .$$

This is a spectral power, i.e., the power contained within a given bandwidth  $(\Delta\omega/\omega)_s$ . It is interesting to compute the coherent power contained within a bandwidth  $\Delta\omega/\omega = \lambda/\ell_c$ , which corresponds to a given coherence length  $\ell_c$ . We call this the coherent power  $P_{\text{coh}}$ , and obtain

$$P_{\text{coh}} = \hbar\omega \left[ \frac{\lambda}{2} \right]^2 \frac{\lambda}{\ell_c} \frac{\mathcal{B}_0}{(\Delta\omega/\omega)_s} . \quad (6.50)$$

Taking  $\ell_c = 1$  micron, Eq. (6.50) becomes in practical units

$$P_{\text{coh}} [\text{watts}] = 7.63 \times 10^{-23} \mathcal{B}_0 / \varepsilon^2 [\text{keV}] .$$

Here  $\varepsilon$  is the photon energy and  $\mathcal{B}_0$  is in units of photons  $\cdot (\text{s})^{-1} \cdot (\text{mm})^{-2} \cdot (\text{mr})^{-2} \cdot (0.1\% \text{ bandwidth})^{-1}$ . Figure 6.8 gives the

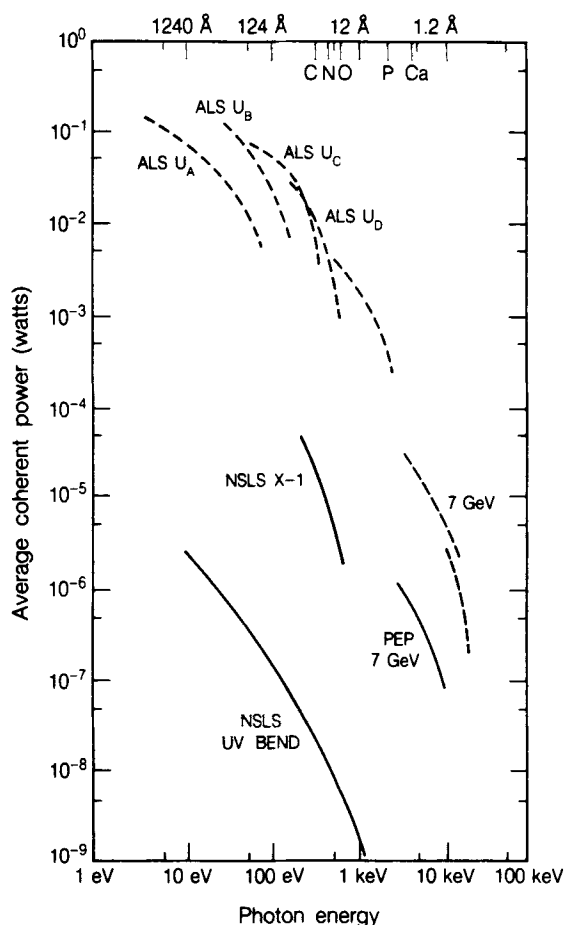


Figure 6.8 Average coherent power in a 1- $\mu$ m coherence length, as a function of photon energy, for several sources of synchrotron radiation.

coherent power from various undulators. Except for a few discrete photon energies where soft x-ray lasers have been operated, undulators operating in high-brightness storage rings appear to be the most assured route to the coherent power for photon energies above a few tens of eV.

### Acknowledgements

I thank Mel Month for encouraging me to complete this work.

## REFERENCES

- Alferov, D.F., Yu. A. Bashmakov, and E.G. Bessonov, 1973, Zh. Tekh. Fiz. **43**, 2126; English translation in Sov. Phys. Tech. Phys. **18**, 1336 (1974).
- Alferov, D.F., Yu. A. Bashmakov, and E.G. Bessonov, 1976, Zh. Tekh. Fiz. **46**, 2392; English translation in Sov. Phys. Tech. Phys. **21**, 1408 (1976).
- Blewett, J.P., 1988, Nucl. Instr. Methods **A266**, 1.
- Born, M., and E. Wolf, 1980, *Principle of Optics* (Pergamon Press, New York, 6th ed.), Chapter 4.
- Coisson, R., 1979, In *European Synchrotron Radiation Facility, The Machine*, edited by D.J. Thompson and M.W. Poole (ESF Strasbourg), 57.
- Coisson, R., and R.P. Walker, 1986, SPIE Proceedings **582**, 24.
- Feynman, R.P., 1963, *The Feynman Lecture on Physics* (Addison-Wesley Pub. Co., Reading, Mass.), Chapter 28, Chapter 32.
- Goodman, J.W., 1968, *Introduction to Fourier Optics* (McGraw-Hill, San Francisco).
- Goulon, J., P. Elleaume, and D. Raoux, 1987, Nucl. Instr. Methods **A254**, 192.
- Green, G.K., 1976, Brookhaven National Laboratory Report BNL-50522.
- Haensel, R., 1988, Nucl. Instr. Methods, **A266**, 38.
- Halbach, K., 1981, Nucl. Instr. Methods **187**, 153.
- Halbach, K., 1983, J. Phys. (Paris) **44**, C1-211.
- Halbach, K., 1985, In Proc. SPIE Intern. Conf. on Insertion Devices for Synchrotron Sources, Stanford, CA.
- Hirai, Y., A. Luccio, and L-H. Yu, 1984, J. Appl. Phys. **55**(1), 25.
- Hofmann, A., 1978, Nucl. Instr. Methods **152**, 17.
- Hofmann, A., 1980, Phys. Reports **64**, 253.
- Hofmann, A., 1986, Stanford Synchrotron Radiation Laboratory ACD-Note 38.
- Jackson, J.D., 1962, *Classical Electrodynamics* (John Wiley & Sons, Inc., New York), Chapter 14.
- Kim, K-J., 1984, Nucl. Instr. Methods **A219**, 425.
- Kim, K-J., 1986a, Nucl. Instr. Methods **A246**, 67.

- Kim, K-J., 1986b, Nucl. Instr. Methods **A246**, 71.
- Kim, K-J., 1986c, In *X-Ray Data Booklet*, edited by D. Vaughn, Lawrence Berkeley Laboratory Pub-490 Rev.
- Kincaid, B.M., 1977, J. Appl. Phys. **48**, 2684.
- Kitamura, H., 1980, Japanese J. of Applied Phys. **19**, L185.
- Kondratenko, A.M., and A.N. Skrinsky, 1977, Opt. Spectrosc. (USSR) **42**, 189.
- Krinsky, S., M.L. Perlman, and R.E. Watson, 1983, In *Handbook on Synchrotron Radiation*, edited by E.E. Koch (North-Holland Publ. Co., Amsterdam), Chapter 2.
- Krinsky, S., 1983, IEEE Trans Nucl. Science **NS-30**, 3078.
- LBL, Conceptual Design Report for 1-2 GeV Synchrotron Radiation Facility, 1986, Lawrence Berkeley Laboratory Report PUB-5172, Rev.
- Moissev, M., M. Nikitin, and F. Fedorov, 1978, Sov. Phys. J. **21**, 332.
- Motz, H., 1951, J. Appl. Phys. **22**, 527.
- Onuki, H., 1986, Nucl. Instr. Methods **A246**, 94.
- Onuki, H., N. Sato, and T. Saito, 1988, Appl. Phys. Lett. **52**, 173.
- Purcell, E.M., 1972, Production of Synchrotron Radiation by Wiggler Magnets, unpublished, reprinted as Stanford Synchrotron Radiation Project Report No. 77/05, 1977, PIV-18.
- Sands, M., 1970, Stanford Linear Accelerator Center Report SLAC-PUB-121.
- Schwinger, J., 1949, Phys. Rev. **75**, 1912.
- Shenoy, G.K., and D.E. Moncton, 1988, Nucl. Instr. Methods, **A266**, 38.
- Sokolov, A.A., and I.M. Ternov, 1968, *Synchrotron Radiation* (Cambridge Univ. Press, Cambridge).
- Synchrotron Radiation News, 1988, (Gordon and Breach) **1**, back cover.
- Wigner, W., 1932, Phys. Rev. **40**, 749.
- Winick, H., 1980, in *Synchrotron Radiation Research*, edited by H. Winick and S. Doniach (Plenum Press, New York), Chapter 2.
- Yariv, A., 1975, *Quantum Electronics* (John Wiley & Sons, New York).